Eur. J. Mech. B - Fluids 20 (2001) 437–470

S0997-7546(01)01129-3/REV

REVIEW ARTICLE

Vortex structures in geophysical convection

H.J.S. Fernando *, D.C. Smith IV

Environmental Fluid Dynamics Program, Department of Mechanical and Aerospace Engineering, Arizona State University, Tempe, AZ 85287-9809, USA

(Received 26 July 2000; accepted 15 September 2000)

Abstract – An intriguing variety of vortex structures arise during buoyant convection, especially in the presence of background stratification and rotation. These vortices play an important role in environmental fluid motions, bearing upon small-scale turbulence to planetary-scale circulation. A brief review of vortex motions associated with buoyant convection is presented in this paper, emphasizing the sources of vorticity, evolution of vortex structures and their role in oceanic and atmospheric dynamics. The genesis of a variety of vortices, for example, mushroom vortices, geostrophic and ageostrophic vortices, dipolar structures and hetons in buoyant convection flows is described, and parameterizations to represent their properties are discussed. New laboratory and numerical simulation results on vortex-related phenomena in stratified and rotating fluids and their implications in geophysical convective flows are also presented. © 2001 Éditions scientifiques et médicales Elsevier SAS

1. Introduction

Motions principally driven and maintained by buoyancy forces are referred to as convection. Since the original study of Count Rumford [1], a large volume of work has been reported on this subject (Siggia [2]; Hunt [3]; Bodenschatz et al. [4]), partly due to its richness in scientific and mathematical contents and to its vast applications in natural and technological flows. For environmental flows, the importance of convection cannot be overemphasized, given that major components of circulation patterns of oceans and the atmosphere are driven by thermally unstable configurations arising from the uneven distribution of solar radiation on Earth's surface. Thermal convective flows can be broadly divided into two classes, depending on the aspect ratio ($A = W/H$) defined by the vertical (H) and horizontal (W) extents of motion. When $A \gg 1$, convection can be treated as horizontally homogeneous, characterized by rising blobs of fluid and compensatory sinking cold fluid elements, as shown in *figure 1(a)* for laminar and turbulent convection cases. Horizontal motions in this case are mainly confined near the upper and lower boundaries. Some examples are the daytime atmospheric convective boundary layer over flat terrain driven by the heated ground ($H \sim 0.5-1$ km and $W \sim 10-100$ km) and the upper-ocean convective boundary layer ($H \sim 0.05$ km and $W \sim 100$ km) generated by nocturnal surface cooling. Conversely, when the buoyancy source is of limited horizontal extent, $A \leqslant \mathrm{O}(1)$, the flow is dominated by horizontal inhomogeneities. *Figure 1(b)* shows examples of cases where the buoyancy source is of limited extent and is either sustained (plumes) or short-lived (thermals). Kindred flow configurations support lateral motions surrounding the convective region, which can take the form of inward mean flows feeding the convective region due to stress gradients (entrainment flow) or outflows driven by horizontal buoyancy gradients (intrusions or detrainment flow). Depending on the flow configuration, a myriad of striking flow phenomena arises in this case.

* Correspondence and reprints.

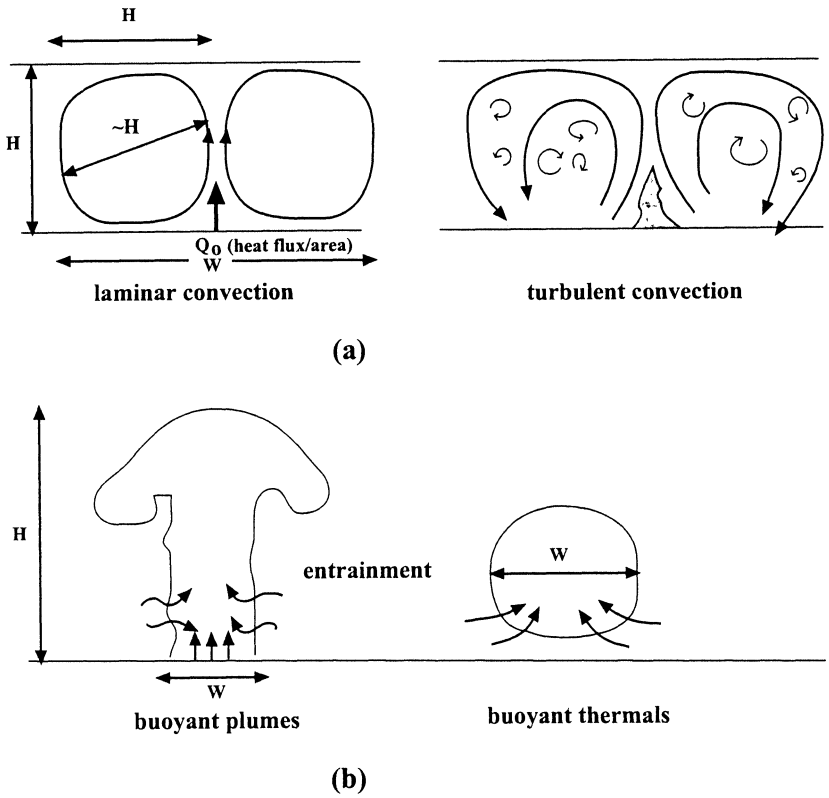

Figure 1. (a) Schematics of laminar and turbulent convection between horizontal boundaries; (b) convection from isolated sources; buoyant plumes and thermals are shown as examples.

Convection occurring in the atmosphere, oceans and solid Earth can be classified according to the scale of motion. On the global (planetary) scale, convection originates in high-latitude oceans wherein cold saline water sinks and deep water spreads over the ocean bottom toward the equator. This plunging water is compensated by vertical mixing and upwelling in low-latitude oceans, thus manifesting thermohaline circulation; a hypothesized flow circuit with convective sinking and upwelling, also referred to as the ocean conveyor belt (Broecker and Denton [5]), is shown in *figure 2(a)*. In the equatorial atmosphere, in the proximity of the inter-tropical convergence zone, vigorous convection penetrates tens of kilometers (deep convection), forming a cumulonimbus belt of clouds (*figure 2(b)*). Here the decrease of pressure with altitude causes rising air parcels to cool and sink, but in so doing they are pushed laterally (poleward) by the rising air from beneath, are subjected to horizontal thermal gradients and generate planetary-scale meridional flow – a building block of Hadley circulation. Although vertical turbulent motions in 'deep convective' cases are not directly affected by Earth's rotation, the plumes within and horizontal flows associated with such regions are significantly influenced by Coriolis forces, leading to flow configurations that are liable to baroclinic instabilities (Eady [6]). In the atmosphere, these instabilities lead to an intriguing class of synoptic-scale vortex phenomena akin to conspicuous weather changes; see the laboratory demonstrations of Fultz et al. [7], Hide and Mason [8], Hide et al. [9], Buzyna et al. [10], and Park and Whitehead [11]. For such large-scale flows, the Rossby number $Ro = u/fL$ based on the characteristic horizontal velocity (u) and length (L) scales and the local planetary vorticity $f = 2\Omega$ (Ω is the background rotational frequency) is on the order $10^{-4} - 10^{-2}$, ensuring that they are rotationally dominated. Furthermore, these flows are highly turbulent, as evident from their large Reynolds numbers $Re = uL/\nu (\sim 10^{12} - 10^{14})$; here ν is the kinematic viscosity. Convection also plays an important role

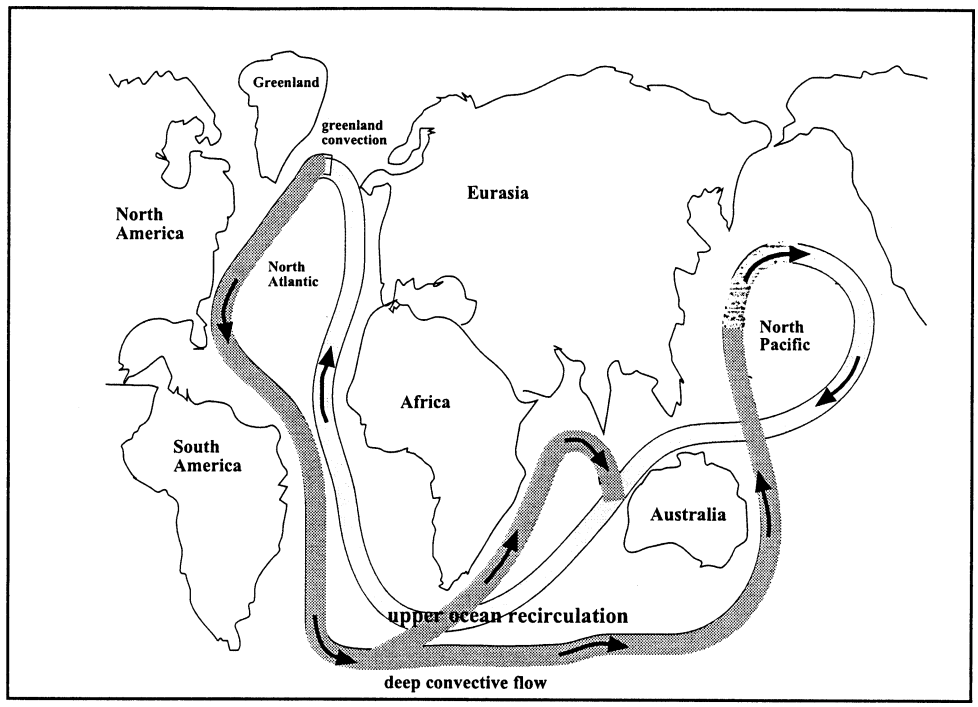

(a)

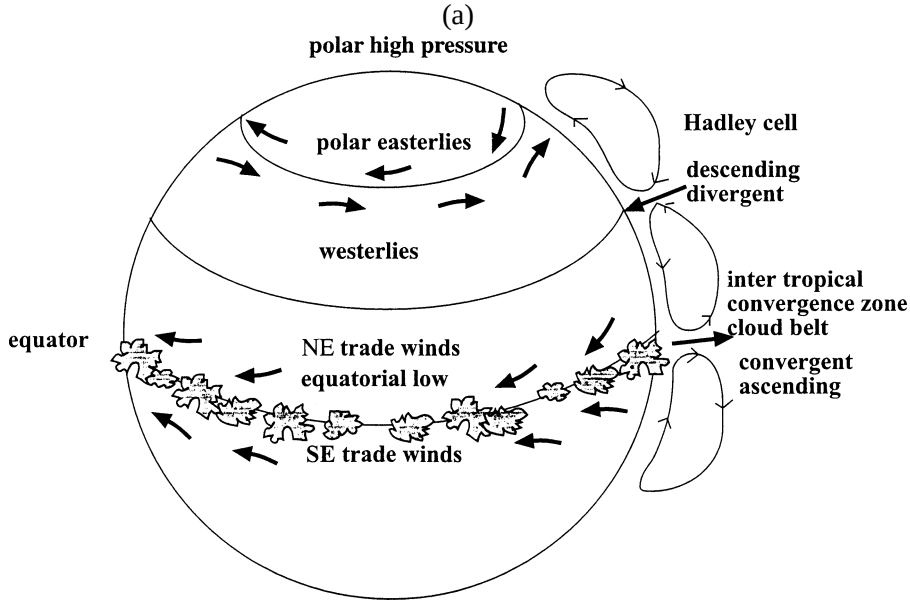

(b)

Figure 2. (a) Thermohaline circulation in oceans; the pathways of convection driven circulation, also known as the ocean conveyor belt, is shown. Deep currents generated due to convection are shown in dark and near-surface flow is shown light; (b) an idealized picture of the global atmospheric circulation powered by convection and attuned by the spatial variation of thermal forcing (due to meridional temperature gradients), stratification and rotation.

in the interior of the Earth, planets and stars (Kim et al. [12]). Convection in basaltic magmas ($H > 100$ m) in temperate and high latitudes of the Earth appears to be turbulent and is rotationally dominated (Griffiths [13]; Davis [14]).

On the meso-scale, salient convection phenomena include thunderstorm cells (see *figure 3(a)*; $W \sim 250-1000$ km, $H \sim 10$ km) and oceanic high-latitude convection (*figure 3(b)*; $W \sim 10-1000$ km and $H \sim 2$ km for regions of deep convection, which are known as 'chimneys'). Also included in this category are polynyas (approximately rectangular or elliptical shaped areas of high-latitude oceans with $W \sim 1-100$ km

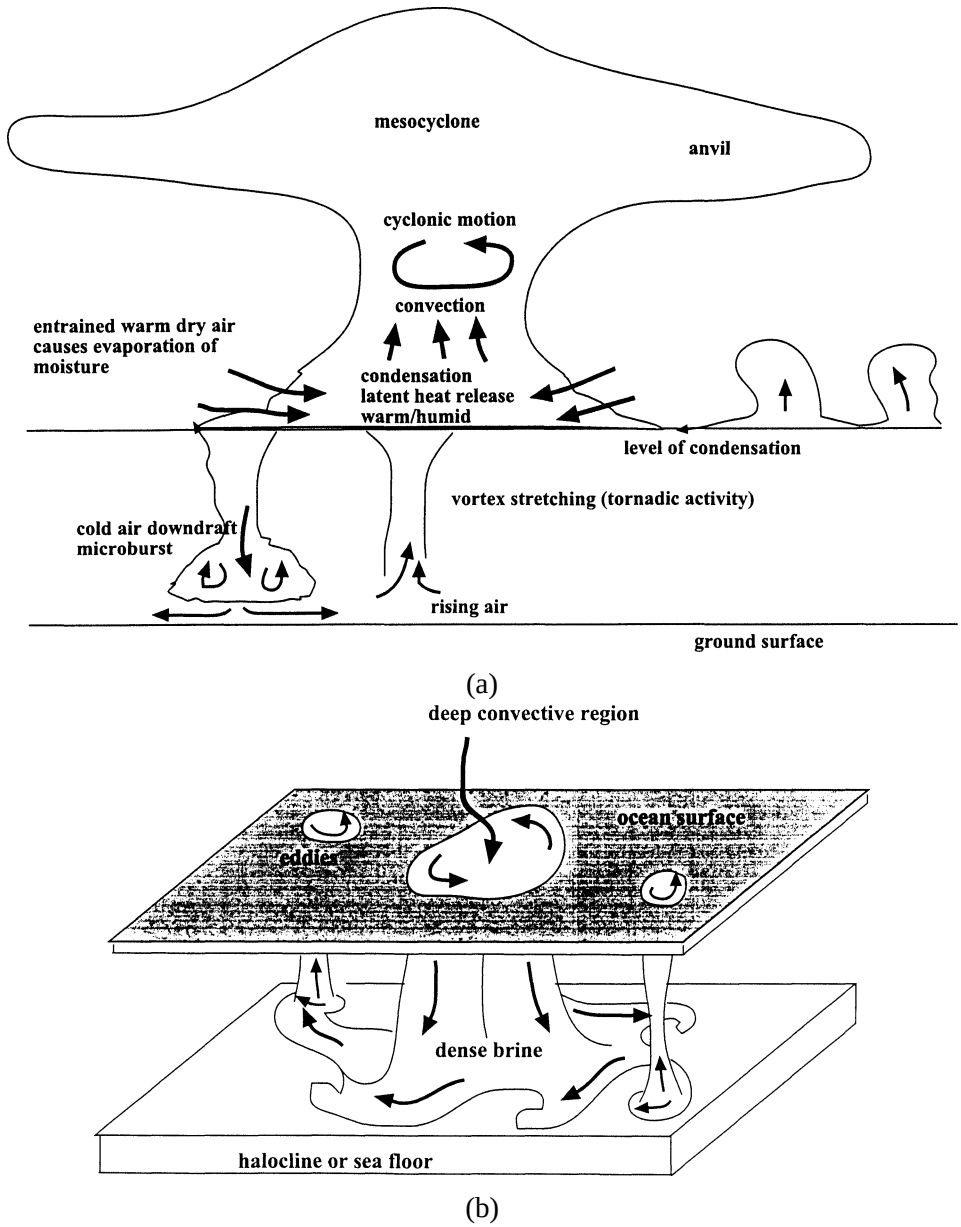

Figure 3. (a) A schematic of a convective thunderstorm and associated vortex structures; (b) a schematic of a convective region (e.g. polynya) in high-latitude oceans (in leads, the open water takes the form of thin long cracks in ice).

and $H \sim 100$ m that remain totally or partially ice free during winters) and leads (thin, long cracks of polar ice cover, 1 m−1 km wide and 1−100 km long). Cooling of open waters in leads and polynyas sets off convection through brine rejection, and sinking fluid parcels reach the pycnocline and spread laterally (Smith et al. [15]; Morison et al. [16]). Unlike in polynyas, convection in leads is shut off within 1–2 days due to the formation of a thin ice layer on the surface. Convective turbulence in polynyas and leads is also unaffected by background rotation, but horizontal flows and plumes within and surrounding them are profoundly influenced by rotation. For a review on meso-scale oceanic convective flows, see Maxworthy [17].

Small-scale (1−10 km) convective features are also prevalent in geophysical flows. A striking atmospheric example is the formation of 'downbursts' or 'microbursts,' which are 0.5–10 km balloons of descending dense air from the middle atmosphere. As shown in *figures 3(a)* and *4*, microbursts originate at the fringes of thunderstorms and pose serious threats to landing aircraft (Fujita [18]). Tornadic vortices (typically 1–10 km) also originate in areas of developing thunderstorms, and are driven and intensified by vigorous convection aloft. Dust devils seen in windy desert areas are intense short-lived low-intensity vortices that are amplified by rising convective elements; heavy loads of dust entrained into their low-pressure centers make them visible. Dust-devil activity on Mars is particularly intense (e.g. in Amazonis Planitia), as evidenced by numerous Martian missions such as Viking Orbiter and Mars Global Surveyor. Dust devils are said to be responsible for most of the soil erosion and some climatic effects on Mars. In the oceanic context, anoxic fluid emitted by submarine hydrothermal vents turbulently mixes with ambient waters and contributes significantly to heat and chemical flux budgets of benthic oceans (Speer and Rona [19]; German et al. [20]; Lavelle and Wetzler [21]).

This paper is intended to review vortex structures appearing in buoyant convection, paying particular attention to the rich variety of vortices appearing when the ambient stratification and background rotation are present. The emphasis will be on geophysical applications, where distinct vortices are ubiquitous and dynamically important. Section 2 presents a discussion on the onset of convection in rotating and non-rotating flows. Section 3 deals with convection in non-rotating fluids as a prelude to the discussion on the horizontally homogeneous rotating and stratified cases given in section 4. Section 5 deals with convection from isolated and distributed sources. Some brief conclusions are given in section 6.

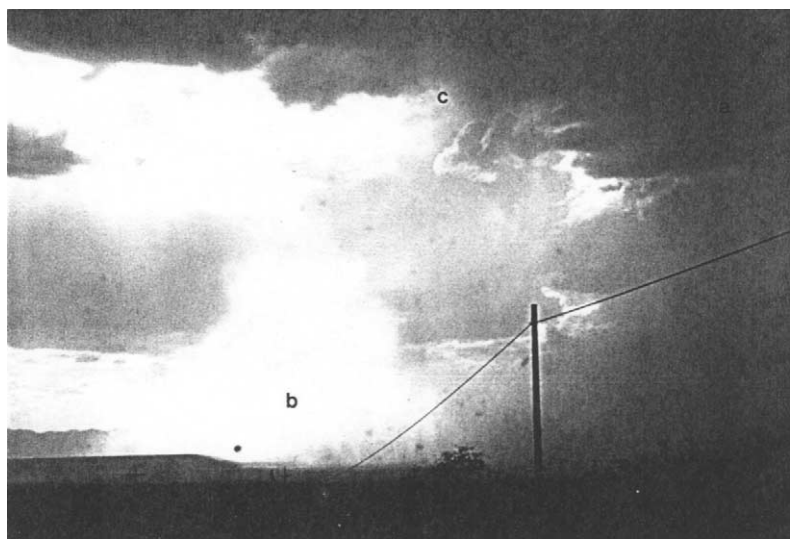

Figure 4. A microburst caught in act during a major thunderstorm in Tucson, Arizona (courtesy, Andjelka Srdic-Mitrovic): (a) Anvil cloud; (b) descending microburst; (c) entraining region of the cloud from where the microburst originated.

2. Onset of convection in horizontal fluid layers

Stability of thermally unstable configurations has been studied extensively since the pioneering work of Rayleigh [22] who considered an unstably stratified fluid layer with temperature gradient $\bar{T}_z$ sandwiched between two horizontal boundaries. Overall, this problem has two governing parameters, the Rayleigh number Ra and the Prandtl number Pr, defined as

$$Ra = g\alpha \bar{T}_z H^4/\kappa\nu \quad \text{and} \quad Pr = \nu/\kappa, \tag{1}$$

where κ is the molecular (thermal) diffusivity, g the gravitational acceleration, α the thermal expansion coefficient of the fluid and H the layer depth. Its linear stability, however, is determined by Ra alone, and the onset of steady convection occurs when Ra exceeds a critical value Ra_c. For example, for stress-free boundaries, the marginal stability curve is determined by the characteristic equation (Chandrasekhar [23])

$$Ra_c = \left(n^2\pi^2 + a^2\right)^3/a^2, \tag{2}$$

where $a = kH$ is the normalized horizontal wave number, and the minimum Ra_c for the lowest normal mode $n = 1$ is given by $(Ra_c)_{\min} = 27\pi^4/4$, corresponding to $a = \pi/\sqrt{2}$. Near this critical value, the flow consists of stationary cells with the horizontal scale on the order of the vertical scale (wavelength $\sim 2^{3/2}H$). Linear analysis does not predict specific horizontal planforms for the marginally stable flow, but allows flow to accept solutions with tessellating symmetric planforms (Thomson [24]). In reality, the wavelength selection is quite sensitive to the initial and boundary conditions used (Koschmieder [25,26]; Theerthan and Arakeri [27]), for example, constant flux boundary condition makes cell patterns much flatter than constant temperature boundary conditions (Sasaki [28]). Non-linear analysis of stability has also been advanced, which shows how the Prandtl number, in addition to the Rayleigh number, influences thermal convection (Busse [29]; Riahi [30]; Fiedler [31]) and the dependence of spatial scales on the degree of non-linearity (Getling [32]; Chapman and Proctor [33]; Rothermel and Agee [34]). Many models exist to describe the evolution of convection (Van Delden [35]), one of the most cited being the model of Lorenz [36] that germinated seed for the strange-attractor theory.

Changes in Ra, however, lead to a host of flow patterns (Krishnamurty [37]). With increasing Ra beyond the critical value, the updrafts, which emerge along the boundaries of polygon-shaped planforms (with size $\sim 2-3H$) for marginally stable flows, tend to concentrate along the hubs of the warm spokes of polygons. This is also called the 'spoke' convection (Willis and Deardorff [38–40]; Busse and Whitehead [41]; Katsaros [42]). Rising warm plumes from these "hot spots" rise to the upper boundary and spread horizontally while downdrafts make up for the lost fluid near the lower boundary. With further increase of Ra, $Ra > 1.6 \times 10^4 Pr^{1.4}$ (for $Pr < 20$), the flow becomes turbulent (Cole and Fernando [43]). Convective turbulent flows have been thoroughly studied, particularly the case of constant buoyancy (or heat) flux q_0 (or Q_0) at the bottom boundary in view of its direct applications to the atmospheric daytime boundary layer. In this case, the flux Rayleigh number $Ra_f = q_0 H^4/\kappa^2\nu$ replaces Ra in (1), where $q_0 = g\alpha Q_0/\rho_0 C_p$, ρ_0 is a reference density and C_p the specific heat. The flow appears to become turbulent for $Ra_f > 10^8$. In dealing with geophysical convection at large Ra_f, laboratory (Niemela et al. [44]), field (Kaimal et al. [45]) and numerical simulation (Kerr [46]; Sullivan et al. [47]) studies have been extremely useful, and daytime convection in the atmospheric boundary layer is being regarded as a case with reasonable understanding in the context of forecasting.

Background rotation increases flow stability and delays the onset of convection (Jeffreys [48]). This is expected in view of the Taylor–Proudman theorem that constrains inviscid fluid motions at low Ro (which ensures vanishing non-linear terms) to two dimensions with no variation of velocity along the axis of rotation. The low Ro condition is satisfied at the onset of rotating convection, but viscous effects allow convective plumes

to emanate from the buoyancy source (e.g. heated plate) as thin sheets and move vertically along the axis of rotation. Nakagawa and Frensen [49] and Chandrasekhar [23] have advanced original linear stability analyses for rotating convection, which show that, in addition to *Ra* and *Pr*, the overall flow is governed by an additional parameter, the Taylor number,

$$Ta = 4\Omega^2 H^4/\nu^2, \tag{3}$$

where Ω is the rate of background rotation. The characteristic equation for the marginal stability for stress-free boundaries is now given by

$$Ra_c = a^{-2}\left[\left(n^2\pi^2 + a^2\right)^3 + n^2\pi^2 Ta\right], \tag{4}$$

with the minimum Ra_c for the $n = 1$ mode being

$$(Ra_c)_{\min} \approx 3\pi^4\left(Ta/2\pi^4\right)^{2/3}, \quad \text{whence } a \approx \left(\pi^2 Ta/2\right)^{1/6} \text{ for } Ta \to \infty. \tag{5}$$

The above results also show that the ratio of temperature gradients required for the onset of convection in the rotating case $(\bar{T}_z)_{Rot}$ is higher than its non-rotating counterpart $(\bar{T}_z)_{Nrot}$, viz.

$$\frac{(\bar{T}_z)_{Rot}}{(\bar{T}_z)_{Nrot}} = 1.3 \times 10^{-2} Ta^{2/3}, \quad \text{for } Ta \to \infty, \tag{6}$$

in consonance with the Taylor–Proudman theorem. Non-linear treatments on the dynamics of rotating convection also have been advanced; for example, Julien and Knobloch [50].

Flow at the onset of rotating convection is clearly different from the non-rotating case, in that the former has initial vertical vorticity. *Figure 5* shows the streamline patterns for a marginally stable case with a hexagonal planform (Chandrasekhar [23]). Note that the rotating case is signified by the presence of vertical vorticity whereas vorticity in the non-rotating case in confined to the horizontal (section 3). As the Rayleigh number is increased beyond criticality and at various Taylor numbers a multeity of structures evolves in rotating convection, and these will be discussed in section 5.

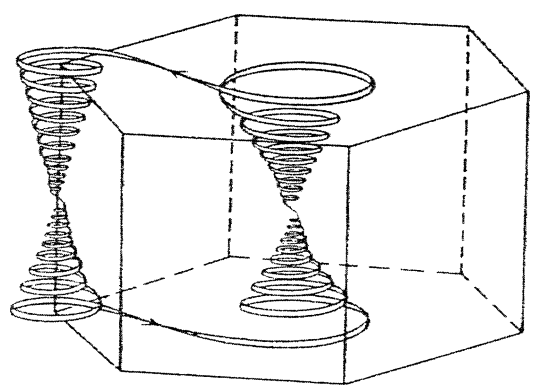

Figure 5. A perspective sketch of the pathlines in a hexagonal cell that develops in rotating convection (from Veronis, as quoted by Chandrasekhar [23]). The fluid rising at the center of the cell feeds the flow at six corners and each corner receives fluid from three adjacent cells.

3. Non-rotating convection in wide horizontal fluid layers

As stated before, convection in thermally unstable configurations between horizontal boundaries has been well studied, covering laminar, transitional and turbulent states (Adrian et al. [51]; Martinet and Adrian [52]). It has been demonstrated that moderately high Rayleigh number convection ($Ra_f \sim 10^7-10^8$) occurs in intermittent bursts (Foster [53]; Foster and Waller [54]) wherein blobs of heated fluid elements (thermals) are sporadically detached, enter the interior of the fluid and are homogenized therein. Motions directly induced by these thermals and fluid that sweeps into fill the void so generated determine the structure of convection. Laboratory experiments show that heated fluid is accumulated in polygon-shaped planforms, migrates toward the vertices and then detaches as thermals (*figure 6*, which shows the results of Willis and Deardorff [55]). A simplified version of this scenario constitutes Howard's [56] model for high Rayleigh number convection, in which the thickness δ of the thermal boundary layer near the heated plate grows until a critical Rayleigh number is reached whence the 'entire' boundary layer breaks down to form thermals. The sizes of the blobs so emanated were found to have the following length and time scales,

$$\lambda \approx 48\left(\kappa^2\nu/q_0\right)^{1/4} \quad \text{and} \quad \tau \approx 14(\nu/q_0)^{1/2}, \tag{7}$$

where the numerical constants are based on the simulations of Foster [53]. Support for Howard's model, mainly qualitative and occasionally quantitative, has also been provided by laboratory experiments (Sparrow et al. [57]; Ginsburg et al. [58]; Katsaros et al. [59]; Foster and Waller [54]). *Figure 7* shows the formation and rise of thermals in a thermal convection experiment. Also shown in the figure is a schematic of the rolling back of the periphery of the thermals to form a mushroom shape, which is due to the baroclinic production of vorticity according to the vorticity ($\tilde{\omega}$) equation,

$$\frac{\partial\tilde{\omega}}{\partial t} + \tilde{u}\cdot\nabla\tilde{\omega} = \tilde{\omega}\cdot\nabla\tilde{u} + \nabla p \times \nabla\frac{1}{\rho} + \nu\nabla^2\tilde{\omega}. \tag{8}$$

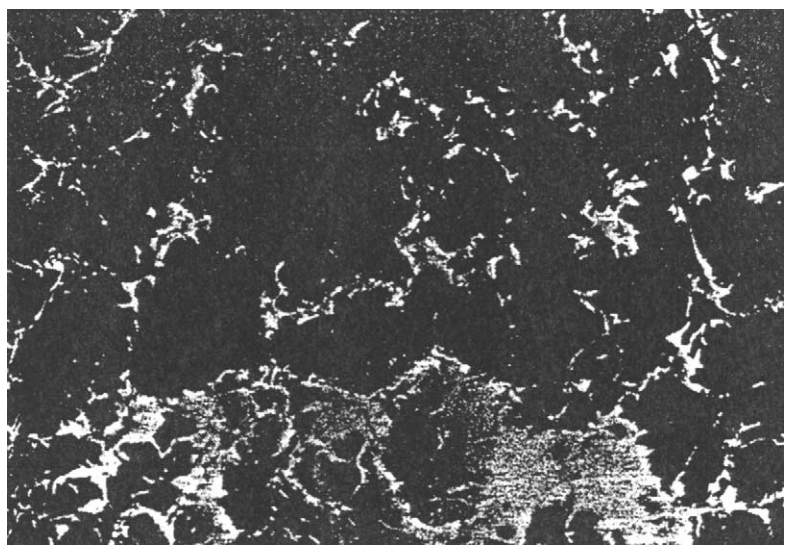

Figure 6. A planform of convection very near the heated boundary of a laboratory tank at $Ra_f \approx 5 \times 10^{11}$. The white lines (dyed by a milk tracer) indicate areas of horizontal convergence (from Willis and Deardorff [55]).

Figure 7. Visualization of 'mushroom' plume vortices rising from a heated plate (from Sparrow et al. [57]).

Given that there is no initial vertical relative vorticity ω_z in the fluid (here z is antiparallel to the gravity) and no major mechanism for its subsequent generation, vortex structures in non-rotating convection are dominated by the horizontal vorticity ω_h. Some relevant examples are the rolls at or near the critical Rayleigh numbers and mushroom and roll vortices at high Rayleigh numbers. In nature, however, horizontal vortex lines, either produced by convection or (mainly) by background vertical shear, can be tipped by the horizontal gradients of vertical velocity induced by turbulent convection itself so that the term $\omega_h(\partial w/\partial x_h)$ causes the development of ω_z according to (8). This is one of the possible generation mechanisms of 'dust devils' and other atmospheric vortices (Maxworthy [60]; Klemp [61]). Dust devils, however, are prevalent in areas of pre-existing vertical vorticity, for example, due to horizontal shear generated by moving vehicles. Earth's rotation plays an insignificant role in developing such vortices (Sinclair [62]).

The role of thermals emanating out of heated surfaces, however, changes with increasing $Ra_f (> 10^9)$, in response to the intensification of convection. Although thermals near the surface may be still developing (Foster and Waller [54]; also see *figure 6*), they are largely effaced by strong convective eddies in the fluid layer (Adrian et al. [51]). Under such conditions, a dynamical balance can exist between the thickening of the unstable thermal boundary layer by diffusion and entrainment of fluid from it by turbulent eddies, as postulated by Fernando [63]. Thence, the thermal boundary-layer thickness becomes $LPe^{-1/2}$, where $Pe = uL/\kappa$ is the Peclet number. Simulations of Akitomo et al. [64] show that the balance between vertical diffusion and horizontal advection may determine the horizontal length scale of high Rayleigh number convection (which is characterized by strong non-linearity). Indications are that the horizontal length scale increases with increasing Ra_f (Rothermel and Agee [34]).

To further investigate the nature of convection at high Ra_f, a new series of experiments were carried using the apparatus shown in *figure 8*; homogeneous, stratified and rotating fluids were employed. The test cell is a 60 cm cubed Plexiglas tank insulated with 2.5 cm thick removable (for flow visualization) Styrofoam boards on the four sides. Insulation was provided on the top to prevent evaporative cooling. The tank bottom was constructed of 1 cm thick Aluminum plate, underneath of which lay custom-built heating pads. Below the heating pads were two layers of (1.25 cm) masonite insulation and a single layer of 2.5 cm foam insulation, respectively. A variable voltage supply was used to regulate the spatially uniform steady (after the decay of initial transients) heat flux to the bottom of the tank. The flow was seeded with neutrally buoyant polystyrene beads, and their movements in planes illuminated by vertical or horizontal light sheets of thickness 0.5 cm were recorded using appropriately placed video cameras. By digitizing consecutive frames of images, the particle velocities and vorticity were calculated using the image processing software, DigImage (Dalziel [65]), with estimated errors

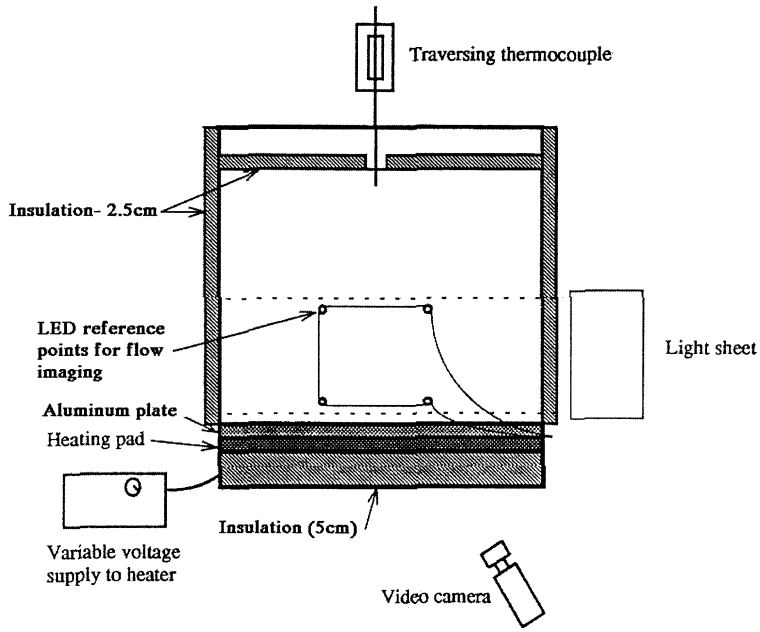

Figure 8. The experimental apparatus used for convection experiments. This apparatus was mounted on a rotating table.

of 10% for velocity and 15% for vorticity. The vertical temperature profiles were made using a set of traversing thermistors.

Figure 9(a) shows the velocity and vorticity fields taken during an experiment with $Ra_f \sim 10^{10}$. The experiments were performed with initial linear thermal stratification, and at the time shown the bottom mixed layer has grown to z $\approx$ 12 cm; here z is measured from the buoyancy source (heated surface) into the convective layer. The flow is now organized into two large cells with opposite sign vorticity, with sweeping motions near the plate capable of effacing the rising thermals. The average cell size ($\sim$ 20 cm) and the scale of updrafts ($\sim$ 5 cm) are much different from the thermal size of 1.2 cm calculated on the basis of (7), indicating that the intermittent thermal bursts have been strongly modified by eddies. Updrafts carry heat from near the surface, which are compensated by downdrafts that occupy a relatively larger area. The r.m.s. turbulent fluctuations within the convective layer, evaluated by horizontally averaging the measured fluctuations at a given z, show that they follow the scaling proposed by Deardorff [66] for turbulent thermal convection, in that the velocity and length scales of turbulence for $z > 0.1H$ become, respectively, the convective velocity $w_* = (q_0 H)^{1/3}$ and convective layer depth H. As an example, the vertical velocity variance obtained in a series of experiments with $10^{10} < Ra_f < 10^{12}$ is shown in *figure 10*, together with the atmospheric field measurements compiled by Fernando et al. [67], laboratory experiments of Adrian et al. [51] and Cenedese and Querzoli [68] and the theory of Hunt [69]. The latter theory predicts the distortion of shear-free turbulence near a solid or strongly stratified boundary. Note that within the error margins the laboratory and field data agree well. The theory of Hunt [69], however, tends to underpredict turbulent intensities.

Hunt's [69] formulation assumes that the nature of convective turbulence near a boundary (e.g. near a density interface) can be represented by direct superposition of homogeneous turbulence and an irrotational flow field. The flow surrounding the turbulent eddies is modified by irrotational motions so as to produce a velocity field that satisfies interfacial boundary conditions. This formulation has been extended to include possible modification of vortex structures at the boundary. The predictions made by the modified model have shown a better agreement with data taken near interfaces, underscoring the importance of vortex dynamics near the

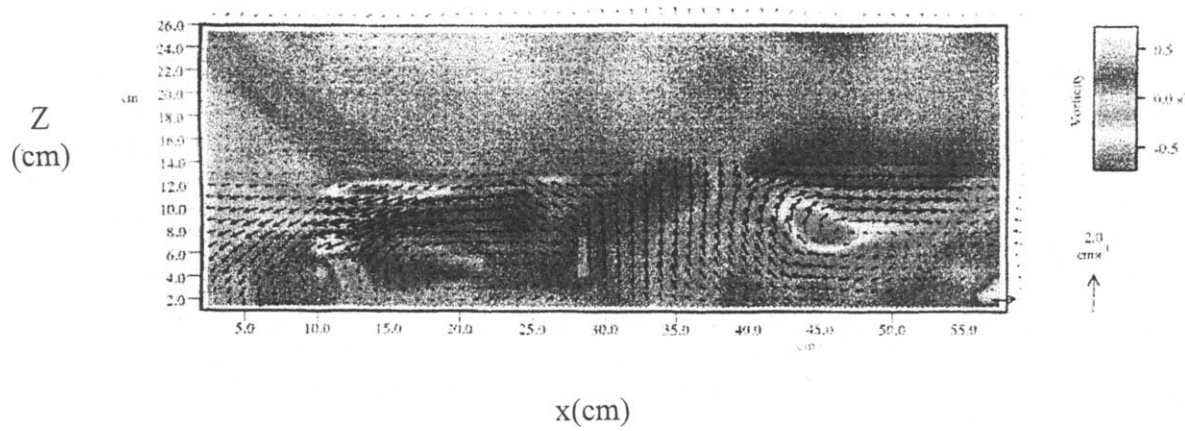

Figure 9. (a) Velocity (shown by vectors) and vorticity (indicated by color) fields obtained during a non-rotating thermal convection experiment initiated with a linear temperature stratification; $Ra_f \sim 10^{10}$; (b) the vorticity and velocity structure near the interface that separates the convective layer from the stratified layer aloft. Only the upper part of the convective layer is shown.

boundary (see Kit et al. [70]). Also note in *figure 10* that there are velocity fluctuations above the convective layer ($z/H > 1$), as a result of the generation of internal waves at the top of the convective layer. *Figure 9(b)* shows the velocity and vorticity structure near the interface between the convective layer ($Ra_f \approx 10^{10}$) and the stably stratified layer aloft (buoyancy frequency 0.6 rad/s), which also indicates how the updrafts penetrate into and generate internal waves in the stratified layer. Similar imprints of plume impingement have been observed in radar studies of atmospheric penetrative convection (Hardy and Otterson [71]). The ensuing vortical perturbations can excite outward propagating internal waves, at times carrying a substantial amount of energy out of the interface (Linden [72]).

Carruthers and Hunt [73] have addressed the problem of internal waves in convective flow configurations (also see Carruthers and Moeng [74] and Perera et al. [75]). They considered a three-layer system, in which the lower convective layer is capped by a strong inversion, having a thickness h and across which the buoyancy

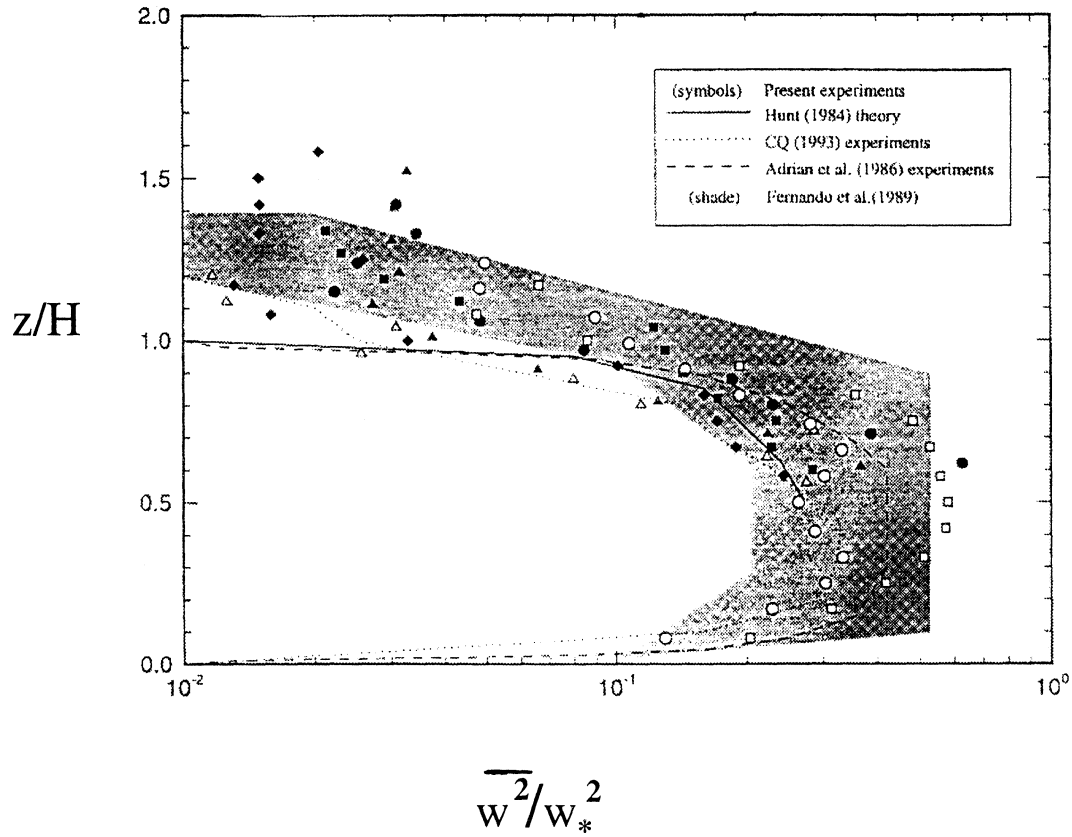

Figure 10. The vertical velocity variance w^2 normalized by the convective velocity, as a function of the distance from the heating surface.

jump is Δb, with an interfacial buoyancy frequency of $N_i = \sqrt{\Delta b/h}$. They showed that entrainment at the inversion is determined by the bulk Richardson number $Ri_b = \Delta b H/w_*^2$ and that internal wave modes produced at the inversion are determined by the internal Richardson number $Ri_I = N_i^2 h^2/w_*^2$. Large Eddy Simulation results show that in the range $13 < Ri_b < 44$ the entrainment at the interface is dominated by the impingement of plumes emanating from the heated boundary, wherein the plumes penetrate into the interface (*figure 9(b)*) and squeeze out wisps of fluid into the turbulent layer (Sullivan et al. [47]). At higher Ri_b, this splashing mechanism disappears and the interfacial mixing is dominated by the breaking of internal waves at the inversion (Perera et al. [75]). Carruthers and Hunt [73]) showed that, for $p^2\pi^2 > Ri_I$,where p is an integer, there exist at most $p$number of wave modes, with the number of modes decreasing with increasing (but weak) stratification aloft the inversion. For example, for $Ri_I < \pi^2$, only one wave mode (flapping or the first mode) of internal waves is possible (McGrath et al. [76]). *Figure 11* shows FM/CW radar returns obtained during the CASES-99 experiment carried out in Kansas during October 1999, where the first mode of waves, which decays upward, is evident. The amount of radiation out of the convective layer via internal waves depends on Ri_I and Ri_b. If the disturbances generated at the interface are energetic enough to grow and break in the generation area, no significant energy can be radiated outward (E and Hopfinger [77]; Perera et al. [75]).

In the Ri_b range plausible in the laboratory, however, interfacial mixing appears to occur by a mechanism whereby the interface is maintained at a marginally (statically) unstable state (Deardorff et al. [78,79]). Consequently, in such flow configurations, also known as the non-penetrative convection, neither a buoyancy jump nor internal waves exist at the interface $\Delta b = 0$. In many geophysical situations, however, an interfacial

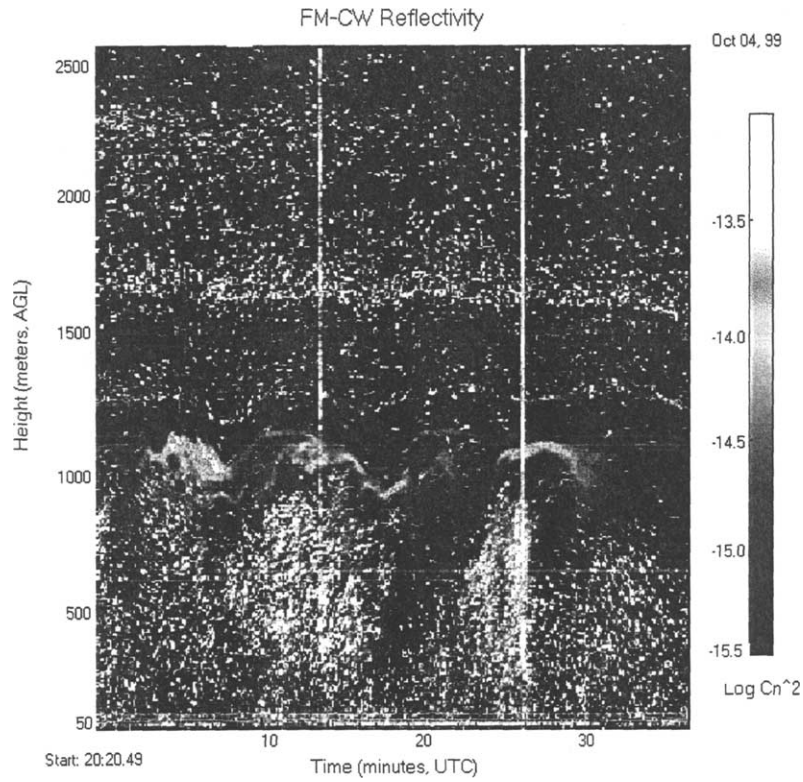

Figure 11. FM/CW radar images of penetrative thermal convection taken during the CASES experiment (courtesy: Microwave Remote Sensing Laboratory, University of Massachusetts). The airborne material and creatures manifest the radar scatter.

buoyancy jump develops at the interface (penetrative convection), allowing plumes to cause mechanical entrainment or internal waves to grow and break as discussed above. The conditions under which the transition from non-penetrative to penetrative convection occurs are yet to be determined.

4. Rotating convection in wide horizontal fluid layers

4.1. Homogeneous fluid layers

Owing to the presence of background rotation (planetary vorticity) as a source of vertical vorticity, convection in rotating fluids, during both linear and non-linear phases of evolution, is rich in vivid vortex structures. In the 'linear' phase of flow development, the vorticity $\tilde{\omega}$ evolution follows

$$\frac{\partial \tilde{\omega}}{\partial t} = f\frac{\partial \tilde{u}}{\partial z} + \nabla \times b\tilde{k} + \nu\nabla^2\tilde{\omega}, \tag{9}$$

which illustrates the production of vertical relative vorticity due to the interaction of planetary vorticity with the divergence of vertical velocity, in addition to the production of horizontal vorticity by buoyancy forces b (i.e. baroclinicity). Thermals emanating from the heated surface provide a good source of vertical motions, which, during rise, are stretched by the divergence of vertical velocity, thereby elongating its length ℓ and reducing its

radius while intensifying the cyclonic vorticity. A simple balance can quantify this phenomenon, viz.

$$\frac{D(f+\omega_z)}{Dt} \sim (f+\omega_z)\frac{\partial w}{\partial z} \sim \frac{(f+\omega_z)w}{\ell} \quad \text{or} \quad \frac{(f+\omega_z)}{\ell} \approx \text{constant} = \frac{(f)}{\ell_0}, \tag{10}$$

where $w = D\ell/Dt$ and ℓ_0 is the initial length of the thermal. In addition, under steady conditions, (9) requires the horizontal cyclonic velocities to decrease with height due to the negative horizontal buoyancy gradient,

$$f\frac{\partial \tilde{u}}{\partial z} \approx -\nabla \times b\tilde{k} \quad \text{or} \quad f\frac{\partial u_\theta}{\partial z} \approx \frac{\partial b}{\partial r}, \tag{11}$$

where u_θ is the azimuthal velocity and r is the radial coordinate. The above phenomena are evident from the streamlines shown in *figure 5*, where the vorticity of buoyant (rising) fluid parcels become increasingly anticyclonic and vice versa. Numerous workers, including Nakagawa and Frenzen [49], Rossby [80] and Bajaj et al. [81], have experimentally investigated linear stability of rotating convection in water and gases. Attempts to produce helical pathlines shown in *figure 5*, however, have had only a limited success (Boubnov and Golitsyn [82]). Various planforms and flow structures have been observed at the onset of instabilities, including rolls, but they become unstable even at slightly supercitical Rayleigh and Taylor numbers, leading to quite complex and facinating phenomena. For example, when *Ta* becomes slightly supercritical, the roll convection becomes unstable and lead to spatio-temporal chaos (known as Küppers–Lortz instability) wherein plane-wave perturbations propagate at an angle to the rolls (Hu et al. [83]; Cox and Matthews [84]).

Experiments of Boubnov and Golitsyn ([85,86]) show wide departure from linear theory predictions under varying degrees of supercriticalities (the ratio Ta/Ra_f has been proposed as a measure of superciticality, with the linear regime occurring at $Ta/Ra_f < 25$). A wide variety of supercritical flow states have been documented, though much is yet to be learnt about their dynamics and transitions. The $Ra_f - Ta$ diagram shown in *figure 12* is an extension Boubnov and Golitsyn [82] and indicates possible states and either empirical or theoretical demarcation criteria separating them.

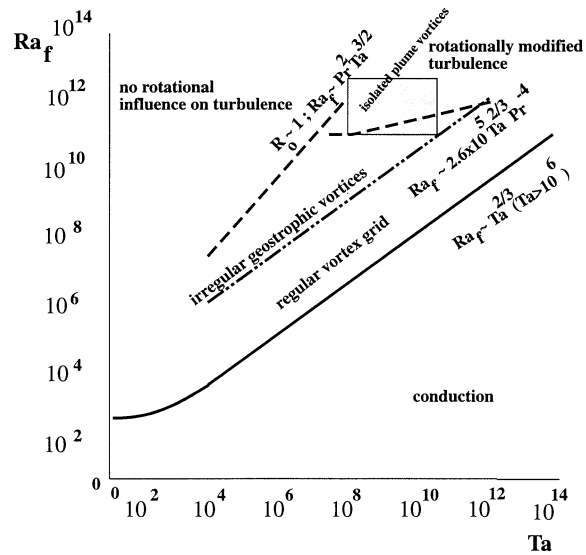

Figure 12. A composite regime diagram indicating possible flow regimes in rotating convection, based on examination of several previous studies. This is an extension of Boubnov and Golitsyn [82].

At slight supercriticalities, the bi-conical structure of linear motions (*figure 5*) breaks down to form a regular vortex grid; *figure 13*, which displays the results of Fultz [87]. The motion field is now governed by the non-linear vorticity equation

$$\frac{\partial(\tilde{\omega}+\tilde{f})}{\partial t}+\tilde{u}\cdot\nabla(\tilde{\omega}+\tilde{f})=(\tilde{f}+\tilde{\omega})\cdot\nabla\tilde{u}+\nabla p\times\nabla\frac{1}{\rho}+\nu\nabla^2\tilde{\omega}. \tag{12}$$

Given the low Rossby number of the flow, the motion field is approximately prescribed by the Taylor–Proudman constraint. As a result, fluid elements tend to rise along thin cylindrical walls, much the same way as that observed in Taylor's ink-wall experiments (Long [88]). The vortical structures emanating from the heated boundary, therefore, consist of thin annular columns of rising warm fluid and cores of descending colder fluid. These vortices are quite stationary, except for occasional vortex mergers (see the arrows in *figure 13*). During the merger process, respective vortices rotate around each other while becoming closer, initiate connection at the top of the vortices while interlacing with each other (Boubnov and Golitsyn [82]). The lateral motion and merger of vortices becomes pronounced with increasing supercriticality (non-linearity), although the general regularity of the vortex grid is still retained. The number of vortices per unit area N_v and the characteristic distance between the vortices d_v during this flow regime are given by (Boubnov and Golitsyn [85])

$$N_v\approx 0.015 f\nu^{-1}Ra_f^{-1/6}\quad\text{and}\quad d_v\approx 7.2(\nu/f)^{1/2}Ra_f^{1/12}. \tag{13}$$

Further increase of supercriticality (*figure 12*) causes the regular grid to transform into an irregular vortex grid (*figure 14*), where the vortices are somewhat weaker, move randomly and merge. Unlike the regular vortex-grid case, these vortices do not extend to the heated bottom boundary, the flow in the vortex core is absent, and the

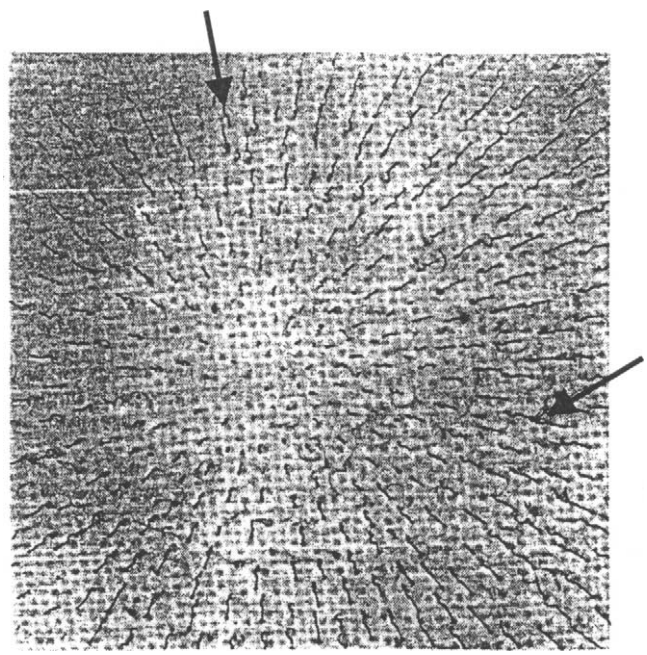

Figure 13. A plan view of an array of convection cells that develop in a rotating fluid layer cooled from the top. Threads of ink from the top surface have moved down the center of each cell. Threads with curlicues at the bottom due to the spiraling motions in each cell are seen head on near the center and obliquely around the periphery. $Ra_f\sim 4\times 10^8$ and $Ta\sim 3\times 10^{11}$ (from Fultz [87]).

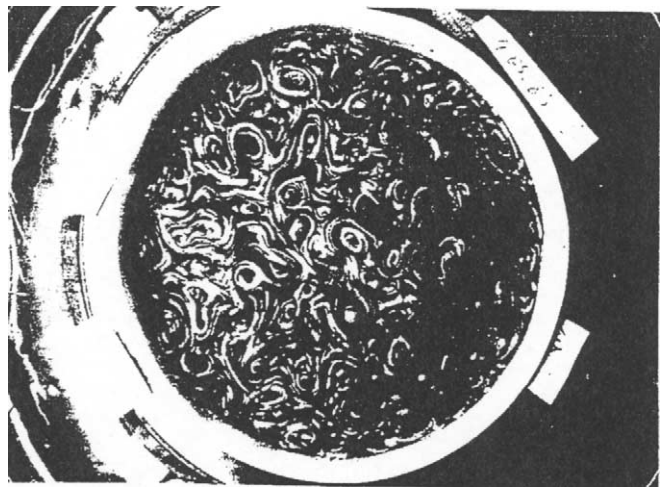

Figure 14. An example of a irregular vortex patterns ($Ra_f \sim 2 \times 10^8$ and $Ta \sim 7.1 \times 10^7$); from Boubnov and Golitsyn [85].

vortices are not strictly vertical. They have been identified as geostrophic vortices (Boubnov and Golitsyn [85, 86]; Sakai [89]) having the velocity scale (Golitsyn [90])

$$u \approx 1.7(\varepsilon/f)^{1/2}, \tag{14}$$

where $\varepsilon = q_0(1 - Nu^{-1})$ is the kinetic energy dissipation rate and $Nu = q_0 H/\kappa \Delta b$ is the Nusselt number based on the buoyancy variation Δb across the convecting layer.

At larger Rayleigh numbers, the irregular vortex regime transitions to a regime with distinct ephemeral vortices, labeled as 'isolated plume vortices'. Unlike the geostrophic vortices, these structures appear spontaneously, are intense, extend to the heated boundary, abide for a short period of time and then fade away, much like dust devils in the atmosphere. The nature of such vortices has been described in the laboratory experiments of Chen et al. [91], Brickman and Kelley [92] and has been studied numerically by Julien et al. [93]; *figure 15*. These vortices undergo intense stretching and merging, indicating strong non-linearity of the motion field. Away from the boundaries, the vortices assume gradient wind balance due to strong curvature of flow paths, viz.

$$\frac{\partial p}{\partial r} = f u_\theta + \frac{u_\theta^2}{r}, \tag{15}$$

with the centrifugal term contributing about 20% of the total pressure gradient. The number density, characteristic diameter and velocity, respectively, of these vortices are (Chen et al. [91]; Brickman and Kelley [92])

$$N_v \approx 1.9 \times 10^{-5} f/\kappa, \qquad D_v \approx 25(\nu/f)^{1/2} \quad \text{and} \quad u_v \approx 0.067(q_0/\kappa)^{1/2}, \tag{16}$$

which differ from the properties of geostrophic vortices given in (13). Certain transport properties of the flow in this 'isolated (ageostrophic) plume vortices' regime have similarities to those of the hard turbulence regime described in Heslot et al. [94] and Castaing et al. [95].

Since isolated plume vortices are in gradient wind balance, they would seem to be stable and inhibit exchange of fluid parcels with the exterior (Julian et al. [93]) unlike the case of their non-rotating counterpart (thermals) where entrainment and detrainment occur (Turner [96]; Ching et al. [97]). Nevertheless, in the rotating case, lateral turbulent fluctuations (with zero mean flow) can exchange warmer fluid of the plume with colder exterior,

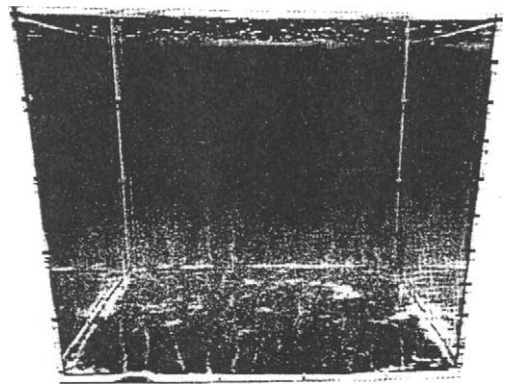

Figure 15. An oblique view of isolated vortices appearing near the bottom heated plate underlying a convecting fluid layer subjected to background rotation ($Ra_f \sim 3 \times 10^{13}$ and $Ta \sim 3.0 \times 10^{11}$); from Chen et al. [91].

causing the dilution of the plume and warming of the background. The horizontal stirring induced by the plumes allows efficient horizontal mixing, but not vertical transports. Therefore, the vertical transport of heat is impeded in this rotating convection regime, leading to an appreciable buoyancy gradient in the region of vortices (Fernando et al. [98]; Julien et al. [93]).

Interposed between these isolated vortices are (incoherent) turbulent motions, which are influenced by the vortices and perhaps affected by Coriolis forces (i.e. the rotationally modified turbulent regime of *figure 12*). Measurements show that convective turbulent motions are affected by background rotation at a height $h_r \approx 12.5(q_0/f^3)^{1/2}$ from the source, whence the r.m.s. velocity and integral length scale, respectively, are given by

$$u_r = 2.4(q_0/f)^{1/2} \quad \text{and} \quad \ell_r \approx 1.1\left(q_0/f^3\right)^{1/2}. \tag{17}$$

Note that these velocity and length scales maintain a constant Rossby number within the convective layer, with $Ro = u_r \ell_r / f \approx 0.75$ (Fernando et al. [98]), although lower (but constant) values of *Ro* have been reported (Ivey et al. [99]; Coates and Ivey [100]). In typical oceanic deep convection regions with $q_0 \approx 5 \times 10^{-7}$ m^{2}s^{-3} and $f \approx 10^{-4}$s^{-1} (Marshall and Schott [101]), $h_r \approx 8.8$ km, and its value is much higher for atmospheric deep convection. Therefore, turbulence generated during deep convection can be considered as unaffected by Earth's rotation.

Rotationally affected turbulence can also play a role in maintaining unstable buoyancy gradients in the convective layer, even away from the region where vortices play a role (Levy and Fernando [102]). The buoyancy scales for rotating and non-rotating convection, b_n and b_r, can be estimated as q_0/w_* and q_0/u_r, respectively, and hence the ratio of pertinent buoyancy gradients can be written as

$$\frac{(\mathrm{d}b/\mathrm{d}z)_{rot}}{(\mathrm{d}b/\mathrm{d}z)_{Nrot}} \sim \frac{b_r/\ell_r}{b_n/H} \sim \frac{H}{h_r} \sim \left(\frac{H^2\Omega^3}{q_0}\right)^{2/3} = R \gg 1, \tag{18}$$

indicating the possibility of dynamically significant buoyancy gradients in the bulk of the convective layer. An important implication thereof is the unsuitability of convective adjustment schemes for numerical modeling of rotating convection.

Figure 16 shows a plot of the dimensionless buoyancy gradient measured as a function of the parameter R, measured using the apparatus shown in *figure 8*. The experiments were conducted on a rotating table and were started after the spin up was completed. The buoyancy gradients were measured using a set of

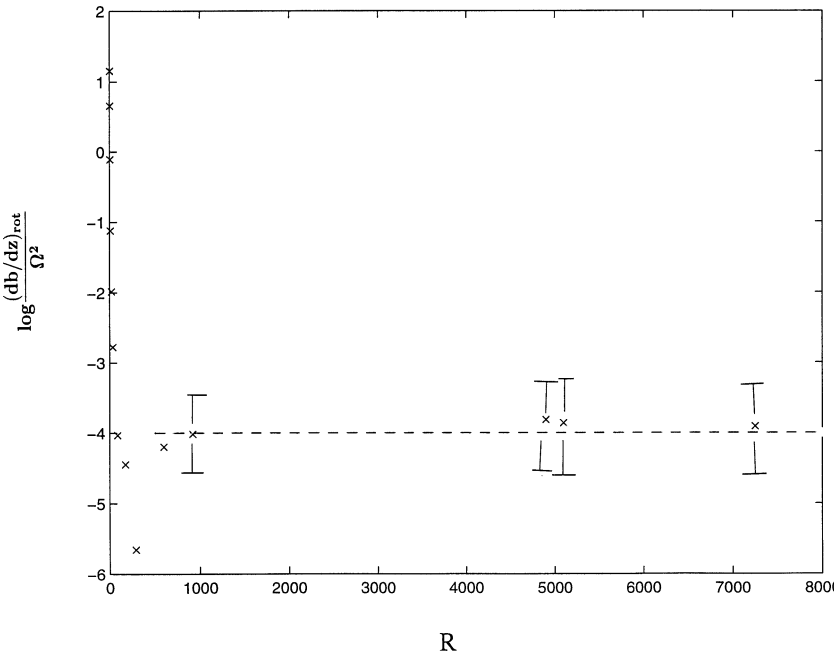

Figure 16. Normalized mean buoyancy gradient in the convective layer as a function of the non-dimensional parameter $R = (H^2\Omega^3/q_0)^{2/3}$. The error bars represent one standard deviation of the average values of more than ten approximately identical experiments.

travelling thermistor probes, with four probes located equidistant from the tank center and attached to a common traversing platform. The results show that the buoyancy gradient assumes a value ($\approx 0.02\Omega^{-2}$) at large $R(> 100$ or so). This buoyancy gradient is much larger than that induced in a non-rotating flow with identical parameters but no rotation. Recent work (Hart and Ohlsen [103]) indicates that the centrifugal buoyancy can also play an important role in determining the buoyancy gradient.

4.2. Stratified fluid layers

A common manifestation in geophysical convection is the penetration of convective mixed layer into a stratified layer in the presence of background rotation. Typical atmospheric ($q_0 \sim 10^{-2}-10^{-3}$ m^{2}s^{-3}, $H \sim 1$ km) and oceanic ($q_0 \sim 10^{-8}-10^{-9}$ m^{2}s^{-3}, $H \sim 50$ m) situations have very high Rayleigh and Taylor numbers, and hence they belong to a regime where convective turbulence is unaffected by rotation (*figure 12*) and where the buoyancy gradient in the mixed layer is unimportant ($R \ll 1$; *figure 16*). However, there are geophysical examples where rotation can have a significant influence on convective layer by influencing the turbulence or through the formation of vortex structures or both. An example is convection in shallow waters of oceans, as illustrated in *figure 17* from D'Asaro et al. [104], for which the typical parameters are $Ra_f \sim 10^{17}$ and $Ta \sim 10^{11}$, which is approximately in the realm of rotationally affected turbulence with isolated vortex formation. This figure also shows the estimated base of the mixed layer during nocturnal cooling of the ocean surface and the trajectories of neutrally buoyant floats deployed within. The float movement is mainly confined to the mixed layer, but occasional 'diving' of floats into some 'cavities' present in the base of the mixed layer can be seen.

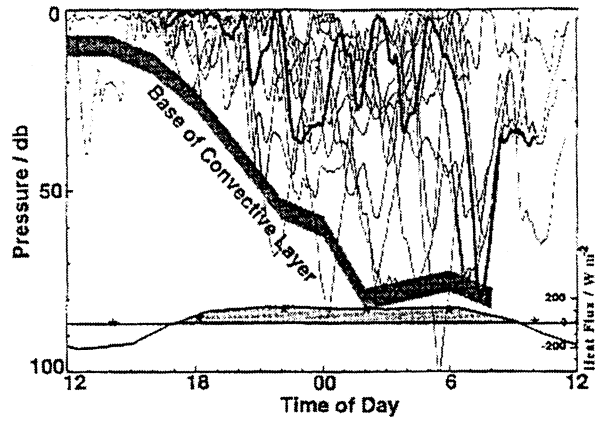

Figure 17. Depth of Lagrangian neutrally buoyant floats deployed in a diurnally varying convective layer in the NE Pacific (D'Asaro et al. [104]). One particular trajectory is shown with a heavier line. The estimated average heat flux (bottom panel) and the average mixed-layer depth estimated from the depth of a very weak maximum in stratification (shaded region) are also shown.

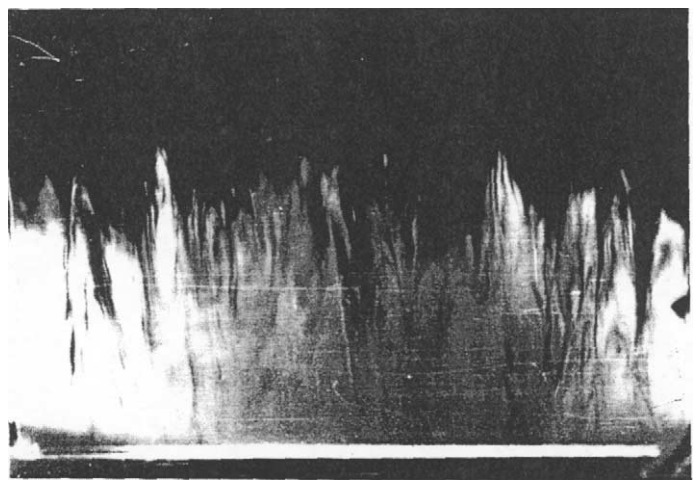

Figure 18. A photograph taken during a rotating convection experiment in a stratified fluid. The convecting layer is added with fluorescent dye for flow visualization.

In order to understand the above phenomenon, laboratory experiments were carried out using the apparatus shown in *figure 8*. The apparatus was mounted on a rotating table, which also supported equipment for flow diagnostics. The convective layer at the bottom was allowed to grow into the stratified layer and the observations were mainly taken in the rotationally affected turbulence regime, within the shaded parameter range marked on *figure 12*. *Figure 18* shows a side-view photograph taken in this regime, indicating how the vortex structures developing near the heated boundary are penetrating into the stratified layer. The flow visualization was performed via injecting dye into the bottom of the convective layer and allowing it to disperse as convection develops. A vertical sheet of light of thickness 0.5 cm was used to illuminate the flow. Note that overall mixing is inefficient and mainly occurs along penetrating vortex structures (i.e. dye distributed well within vortices), and this observation is broadly consistent with the numerical simulations of Julian et al. [93,105]. Accordingly, lateral mixing is taking place through the horizontal exchange of fluid parcels across vortex boundaries, but the net entrainment into the plumes is negligible and hence plumes do not grow laterally with the distance from the bottom. Cavities are developed as a result of the penetration of these slender vortices into the stratified

layer aloft, allowing intermittent penetration of floats beyond the averaged location of the mixed layer base as shown in *figure 17*. The corresponding penetration depths of thermals in the non-rotating case are much smaller (Deardorff et al. [79]).

The averaged height of the mixed layer along a given illuminated vertical section of the tank was calculated by estimating the 'edge' of the convective mixed layer using the standard laser-induced fluorescence technique. In this method, the illuminated region was video taped, and the mixed-layer base for each frame was estimated by scanning each vertical line of pixels to identify the location where the fluorescent intensity changed by a factor of five from the background value. The line joining such location of each pixel column was considered as the base of the convective layer in the plane of visualization. The mean mixed-layer depth (H) as well as the r.m.s. variation of the mixed-layer thickness (δ_p) from the mean value, which was defined as the depth of the vortex induced cavities, were then calculated.

The governing variables for the problem are the buoyancy frequency of background stratification N, w_*, Ω, and H, which can be used to obtain the relevant dimensionless parameters, the Richardson number $Ri_N = N^2H^2/w_*^2$ and the Rossby number $Ro = w_*/\Omega H$. (Molecular parameters can be neglected, considering the turbulent nature of the flow). Experiments were conducted by varying one non-dimensional parameter at a time while holding the others, and the results showed the following correlation

$$\frac{\delta_p}{H} = 13.5 Ri_N^{-3/2} Ro^{-1}, \tag{19}$$

as depicted in *figure 19*. Application of (19) to the field observations of *figure 17* with estimated values $Ri_N \approx 12.7$, $Ro \approx 6$ and $H \approx 50$ m yields a characteristic penetration height of $\delta \approx 2.5$ m, which is consistent with the limited observations of individual float penetrations evident in *figure 17*.

Further support for the above laboratory results was provided via numerical simulations carried out by salinating the surface of a stably stratified region of the ocean. The simulation was carried out in a domain of 7.5 × 0.1 km, with a grid resolution of 30 m ×5 m. The forcing was specified by an unstable surface

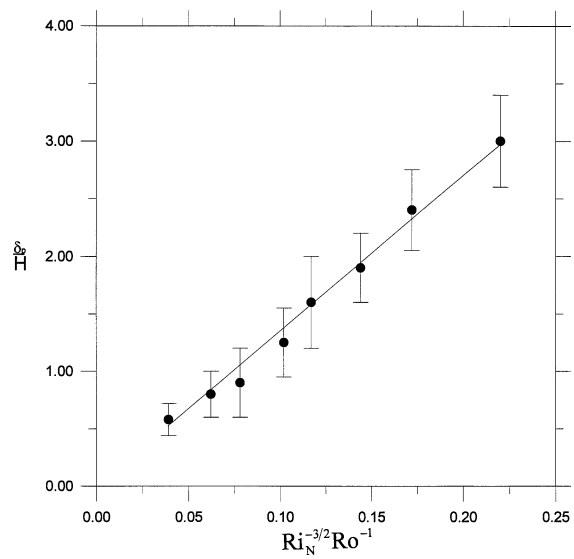

Figure 19. A plot of the non-dimensional characteristic penetration depth of floats δ_p/H in a convecting mixed layer (the r.m.s. variation of the convecting layer height about its spatial mean) as a function of $Ri_N^{-3/2}Ro^{-1}$.

buoyancy (salinity) flux of 5×10^{-7} $m^2 s^{-3}$, distributed along a 6.75 km line segment at a latitude of 80°. The upper layer (thickness 40 m) was well mixed, and was separated by the bottom layer of thickness 10 m by a halocline of thickness 40 m and buoyancy frequency 0.0021 rad s^{-1}. The numerical model used is described in Smith and Morison [106]. It is a non-hydrostatic finite difference model for the upper ocean, based on the momentum equations for an incompressible Boussinesq fluid,

$$\frac{\partial \tilde{u}}{\partial t} + \tilde{u} \cdot \nabla \tilde{u} + \frac{1}{\rho_\circ} \nabla \mathrm{p} + \tilde{f} \times \tilde{u} = A_\mathrm{I} \nabla^4 \tilde{\mathrm{u}} - \frac{\tilde{\mathrm{k}} \mathrm{g} \rho}{\rho_\circ}, \tag{20}$$

with the conservation of salt expressed as

$$\frac{\partial (S)}{\partial t} + \tilde{u} \cdot \nabla (S) = K_I \nabla^4 (S), \tag{21}$$

where A_I and K_I are biharmonic diffusivities of momentum and scalar, respectively, and ρ is the density. The equations were solved by taking the divergence of the momentum equation to yield an elliptic equation for pressure, which was solved at each model time step. No slip side-wall and upper boundaries were used for the simulations, and the lateral boundaries were kept far from the region of interest. Details of this model formulation are provided in Brugge et al. [107] and Smith et al. [108]. A source term distributed salt over the upper several grid cells of the model, as in Smith and Morison [106], and this buoyancy flux was maintained

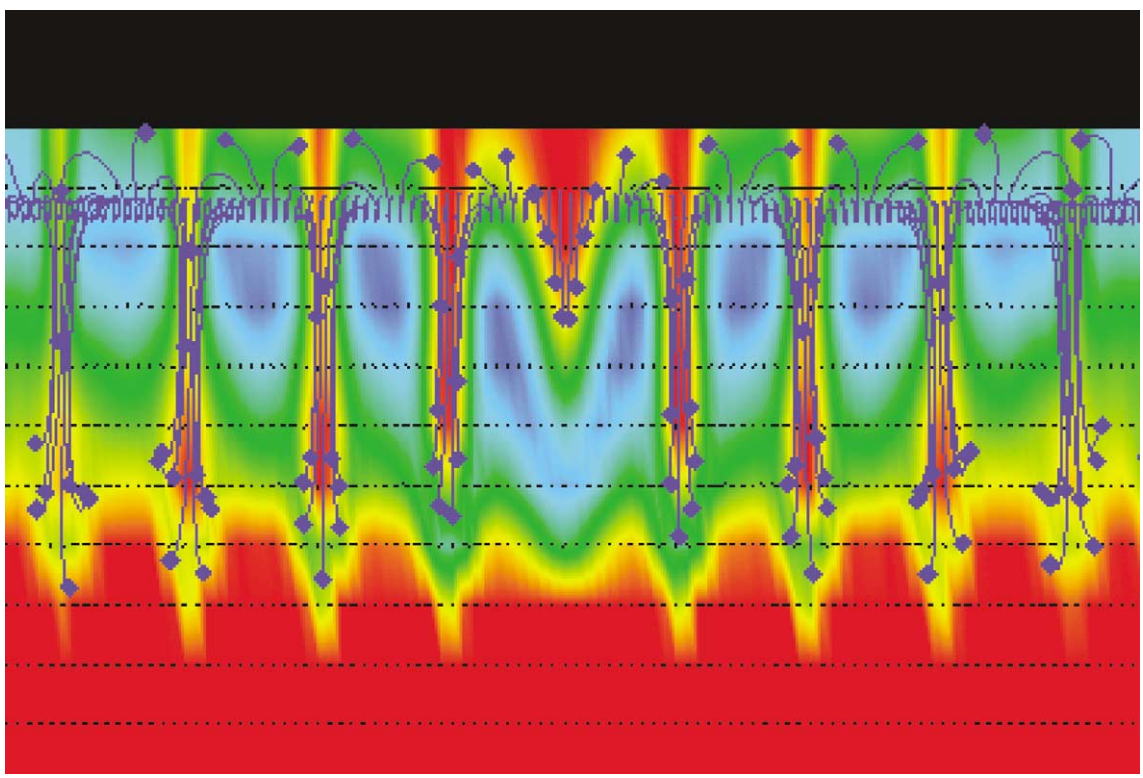

Figure 20. Numerical simulation of convection from a distributed buoyancy source in polar oceans and the trajectories of neutrally buoyant numerical floats introduced in to the convecting layer. The tracers were released at time $t = 0$ at a depth of 5 m. The range of colors spans 31 to 31.04 ppt in salinity, with red representing the highest.

constant in time. Constant biharmonic dissipation and diffusion coefficients were used for sub-grid scale representation of small-scale mixing, which were set to minimum values necessary for numerical stability, $K_I = A_I = 2 \times 10^3$ m^{4}s^{-1}. Lavelle and Smith [109] have shown that the details of sub-grid scale turbulence closure (Smagorinsky in that study) are important in getting quantitative agreement for descending plume events in numerical and comparable laboratory experiments. In the present study, where the emphasis is on the variability in qualitative sense, the inclusion of higher-order closures, such as Smagorinsky parameterization, was deemed unnecessary.

Figure 20 shows the density field within the flow domain, which indicate the formation of well-defined vortices that penetrate into the stratified layer. Also shown are the tracks of neutrally buoyant numerical floats released into the convective region from a line source located at a depth 5 m below the surface. The trajectories were calculated by a code provided by S. Lamont of the National Center for Microscopy and Imaging Resources, UCSD. The trajectories are projected onto the plane of visualization. Note the penetration of floats into the undulations created by vortices penetrating into the stratified layer. The laboratory and numerical results presented above lend support for the notion that the anomalous penetration of neutrally buoyant floats observed in *figure 17* can be attributed to the vortex structures of convection.

5. Convection from distributed sources of limited extent

Convection occurring in nature is delimited by finite spatial extent of forcing, and in some cases the aspect ratio A is small enough for lateral motions to play an important role in the dynamics of convection. The idealized case of $W \to 0 (A \to 0)$ corresponds to point/line plumes or thermals, studies of which are useful building blocks in understanding natural flows. Point (line) plumes are described by the total buoyancy flux (buoyancy flux per unit length) emanating from the source, $q_0^p (q_0^l)$ and point (line) thermals are described by the total buoyancy (buoyancy per unit length) released at the source. The dynamics of point and line thermals and plumes in homogeneous and stratified flows has been extensively reviewed in the literature (Fischer et al. [110]; List [111]; Turner [112]; Davies and Neves [113]) since the pioneering work of Morton et al. [114]. Much of the literature on cases with background rotation, however, is recent, and can be attributed to the increased emphasis on oceanic leads, polynyas, deep convection as well as hydrothermal vents in recognition of their climatic implications.

Figure 21(a), (b) shows the behavior of a point plume released into a homogeneous rotating fluid. Given that the source is specified by q_0^p and the other governing parameters being the background rotation Ω and the time of evolution t, any property of the plume, for example the depth of penetration h_p, can be written as $h_p = (q_0^p t^3)^{1/4} f_1(\Omega t)$ where f_1 is a function. Experiments show that at small times ($\Omega t \ll 2.5$) the plume descent occurs as if there is no rotation, i.e. $f_1 \approx 1.8$, indicating an plume descent law of the form $h_p/(q_0^p/\Omega^3)^{1/4} \approx 1.8(\Omega t)^{3/4}$. The decent is slowed beyond $\Omega t \approx 2.5$ or at depths greater than $h_{c1} \approx 3.3(q_0^p/\Omega^3)^{1/4}$; see *figure 21(b)*. The width of the plume (not shown), however, continues to increase until $\Omega t \approx 5.5$ or a plume depth of $h_{c2} \approx 6(q_0^p/\Omega^3)^{1/4}$ is reached. The plume width becomes constant thereafter, indicating the suppression of entrainment and plume turbulence by rotation (Fernando et al. [112]). The entrainment flow persists at plume depths $z < h_{c2}$, but since the descent rate of the plume front is decreased the entrained fluid tends to accumulate above the 'shoulder' of the plume above the depth h_{c2} as evident from *figure 21(a)(ii)*. Consequently, the plume gradually transforms into a cylindrical cyclonic vortex (Boubnov and van Heijst [116]; Spear and Marshall [117]), within which smaller, slender vortices are also evident. Owing to Coriolis effects, the exterior entrainment flow deflects to form a cyclonic vortex, as evident from the time-exposed circulation patterns shown in *figure 22(i)*. After some time, this vortex breaks down to form subsurface cyclonic eddies, the size of which scales with the width of original cyclonic circulation (*figure 22(ii)*). The

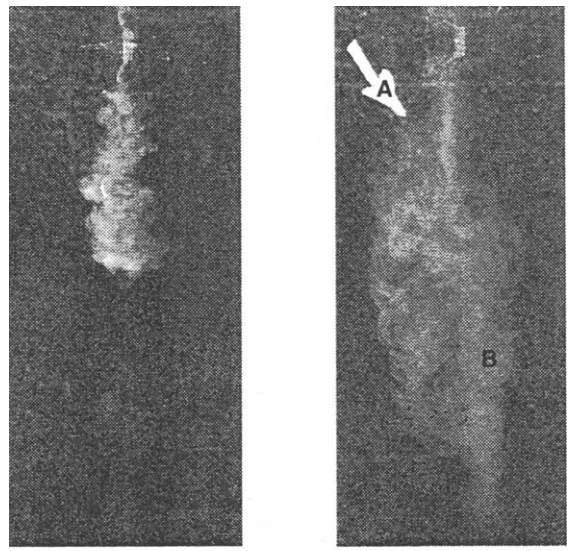

(a)

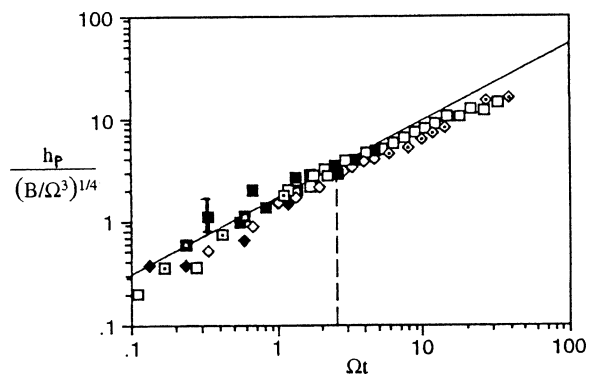

(b)

Figure 21. (a) Photographs of a plume descending into a rotating fluid (from Fernando et al. [116]). The descent (i) before the plume is affected by rotation, and (ii) after the influence of rotation sets in. Also marked are: A – the rise of plume fluid above its 'shoulder' to supply the entrainment demand, and B – Organization of plume fluid into vortex structures; (b) the variation of the normalized depth of plume with normalized time.

genesis of eddies, therefore, can be attributed to barotropic instabilities. (For discussions on the counterpart of thermals in rotating fluids, see Ayotte and Fernando [118] and Helfrich [119]). An interesting sequence of events takes place when the plume reaches a bottom boundary, for example, the presence of a wall or a density interface, as described below.

Figure 23 shows the impingement of a descending plume on a solid boundary in a laboratory experiment, whence the plume deflects and propagates horizontally to form a radial gravity current. Coriolis forces, however, induce an anticyclonic circulation within this outflow, thus generating frontal shear and ultimately breaking down the current to form a series of anticyclonic vortices (Helfrich and Battisti [120]), as seen in *figure 23*. Measurements reveal that the size of eddies generated as well as the length scale of the current at which eddies are formed scale with the Rossby deformation radius, pointing to baroclinic instability as

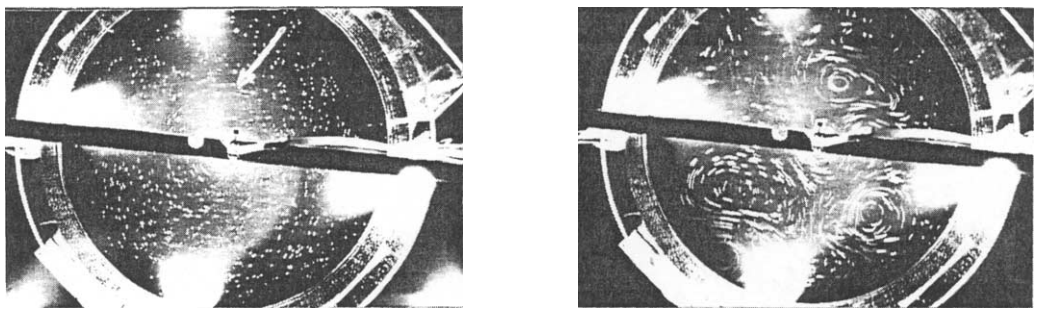

Figure 22. A plan view of a flow configuration similar to that is shown in *figure 21*. The background fluid is seeded with neutrally buoyant tracer particles. (i) The appearance of rim currents (see the arrow) and (ii) breakdown of the rim currents into isolated cyclonic vortices. Details are given in Fernando et al. [116].

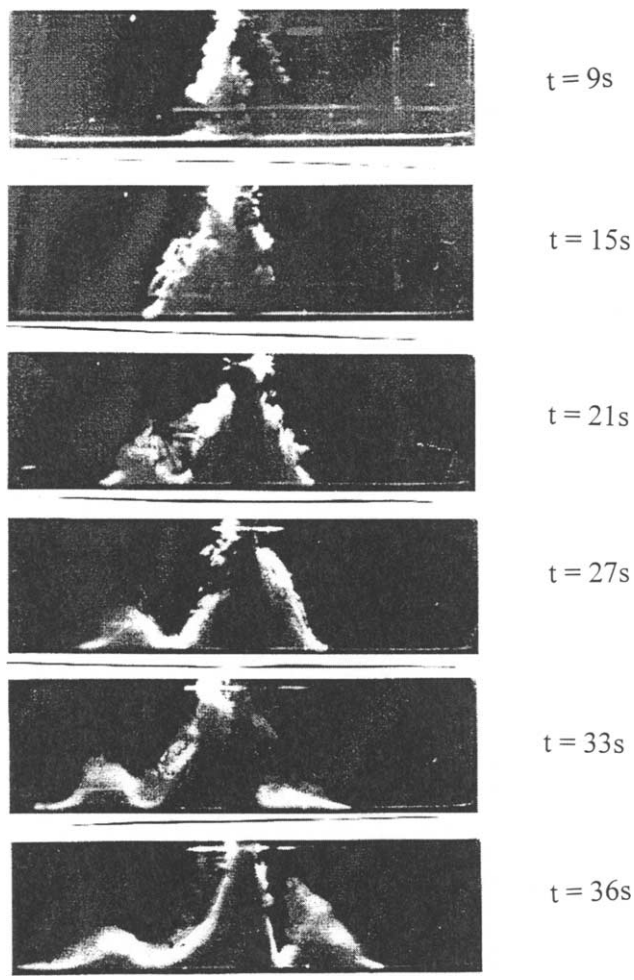

Figure 23. A sequence of side-view photographs showing the evolution of a point plume in the presence of background rotation. $\Omega = 0.5\ \mathrm{s}^{-1}$, $q_0^P = 14.7\ \mathrm{cm}^4\mathrm{s}^{-3}$ and $H = 16$ cm. A section through the plume is illuminated. The times of photographs are indicated; from Fernando et al. [116].

a possible instability mechanism. When eddies are formed away from solid boundaries, they can achieve approximate geostrophic balance, with the ratio of the eddy radius R_e to the height h_e being proportional to N/f or yielding a Prandtl ratio of $Nh_e/R_e f \approx (0.45-0.8)$. At solid boundaries, viscous effects becomes important and eddies become strongly ageostrophic.

Cyclonic vortices generated near the surface and anticyclonic vortices formed at greater depths by the breakdown of the radial outflow interact to form a system of vortices in which the rotation varies from anticyclonic in the dense lower layer to cyclonic in the lighter upper layer. This is evident from the plan views of the experiments of *figure 23*, which are shown in *figure 24*. Here the flow visualization has been performed by seeding neutrally buoyant particles in the homogeneous lighter fluid and by coloring the denser plume fluid with fluorescent dye. (The flow direction of particle streaks is from dot to dash, obtained by systematically chopping the light beam arriving at the camera.) Note the approximate vertical alignment of the cyclonic and anticyclonic vortices.

The vortices described above belong to the class of 'Hetons' (Hogg and Stommel [117]). The thermal wind balance maintains the vertically varying circulation of these vortices, and the interface between lighter upper and dense lower parts of the Hetons domes up to maintain the geostrophic balance; the doming up is clearly seen in *figure 23*. Hetons are recognized as a mechanism of horizontal buoyancy transport in oceans. When they travel horizontally, due to doming of the interface, more fluid from the upper layer is transported than that from the lower layer, thus producing a net lateral flux. Helfrich and Battisti [120] and Fernando et al. [115] have reported the formation of Hetons during convection from point plumes released into rotating fluids.

When the buoyancy source is distributed (with a diameter d_0), then point plume approximation becomes invalid. Far from the source, however, the memory of source dimensions is lost and the plume evolution resembles to that of a point plume. Laboratory experiments show that the point-plume approximation is valid only at distances greater than about $10d_0$ from the source, and d_0 is an important governing variable near the source (Fernando et al. [115]). For example, the velocity scale near the source is given by $(q_0 d_0)^{1/3}$ based on the buoyancy flux per unit area q_0 (Colomer et al. [122]). Deardorff's [66] free convection scaling for horizontal homogeneous convection (section 3) fails here due to the initiation of lateral entrainment flow, which occurs at a time $1.2(d_0^2/q_0)^{1/3}$ after the plume initiation (Colomer et al. [122]). As in the case of point plumes, the presence of rotation leads to a near-surface rim current that breaks down to form cyclonic vortices and the outflow at greater depths carrying dense fluid becomes unstable to form anticyclonic eddies (Jones and Marshall [123]; Maxworthy and Narimousa [124]; Narimousa [125]). It should be noted that the evolution of distributed plumes in rotating fluids depends on the relative magnitudes of d_0 and the characteristic Rossby deformation radius

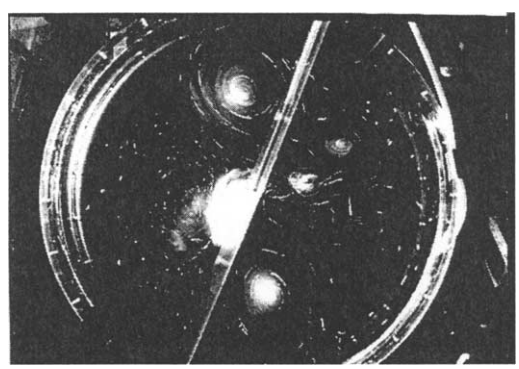

Figure 24. A plan view of an experiment similar to that is shown in *figure 23* but with $q_0^p = 17.8\ \mathrm{cm^4 s^{-3}}$. Note the locations of the cyclonic vortices (marked by neutrally buoyant tracer particles) and anti-cyclonic vortices (fluid dyed with fluorescent dye).

L_R. When $d_0 < L_R$, the plume evolution is expected to be similar to the point source case described above. Conversely, when $d_0 > L_R$, the distributed plume is baroclinically unstable from the outset, and the plume evolution is dominated by the lateral eddy shedding.

Whitehead et al. [126] and Visbeck et al. [127] have argued that, in areas of oceanic deep convection, the input of unstable buoyancy flux at the surface is balanced by the lateral removal of flux by eddies ejected out of the convecting region. It was suggested that this balance is key to the determining of the convective-layer depth. Alternative explanations also exist to predict the depth of convection based on the inhibition of vertical growth by the stratification (Colomer et al. [128]), and future studies should be aimed at firmly establishing the role of eddy transport and principal buoyancy balances pertinent to the regions of oceanic convection.

Polynyas and deep convection regions of high latitude oceans can be construed as driven by distributed buoyancy sources of finite extent. In order to study such cases, the model described in section 4.2 was adopted to simulate a 12 km-diameter polynya, forced for 10 days by a surface buoyancy flux of 2×10^{-7} m^{2}s^{-3} in a domain of 30 km $\times$30 km $\times$300 m. The computational resolution was 5 m in vertical and 240 m in horizontal. *Figures 25(a)* and (*b*) show the plan-view appearance of vortex structures after 2.5 days of simulation, where vorticity at the surface and 225 m depth are shown. *Figure 25(c)* depicts the side view of the salinity distribution, on which the instantaneous velocity vectors corresponding to the visualization plane (u, w) are superimposed. *Figure 25(d)* shows the plan view of the salinity structure at 225 m, together with the horizontal velocity vectors. Note the development of a general cyclonic circulation near the surface, which becomes unstable and breaks up into cyclonic vortices of size ~ 4 km near the surface. Near the bottom, the outflow region breaks down to form anticyclonic eddies. Numerical simulations confirmed the formation of heton-like vortices, much like those observed in laboratory experiments. Legg and Marshall [129] have modeled the lateral spreading of deep convective regions using an ensemble of such hetons.

Impetus for studies on line plumes in rotating environments has been provided by their relevance to polar leads. Winter leads are thin, long cracks of polar ice cap that exposes underlying water to intense atmospheric cooling (*figure 3(b)*). Refreezing of leads occurs within days, during which plumes of dense brine descend from the surface. Laboratory studies of Fernando and Ching [130,131] show that, upon release, the plumes descend for a time $t \approx 2.2\Omega^{-1}$ without being affected by rotation, during which its vertical length grows according to $h_p \approx 1.2(q_0^l t^3)^{1/3}$. Much like point plumes, the vertical growth of line plumes is retarded at a height $h_R \approx 7(q_0^l/\Omega^3)^{1/3}$, and the horizontal growth is inhibited at the width $1.1(q_0^l/\Omega^3)^{1/3}$ after a time $t \approx 2.7\Omega^{-1}$. Coriolis forces deflect the initial entrainment flow so as to generate along-axis counter currents on either side of the plume. The shear across the plume so generated breaks down the counter current system into cyclonic vortices. The mechanism of this vortex generation (whether baroclinic or barotropic) is yet to be identified, but the vertical and horizontal shear surrounding the plume certainly act as sources of energy for instabilities.

Interesting phenomena arise when the vertical development of a line plume is constrained by background stratification and/or rotation. Upon discharging into a rotating uniformly stratified fluid of buoyancy frequency N, the plume rises to its neutrally buoyant level $h_N \approx 3(q_0^l)^{1/3}/N$(when $h_N < h_R$) and then spreads horizontally until the radial flow becomes unstable and sheds off anticyclonic (geostrophic) eddies, as shown in *figure 26* (Bush and Woods [132–134]). In polar oceans, the stratification is not uniform, and can be approximated to a two-layer fluid with weakly stratified upper (~ 50 m) and lower layers separated by a strong pycnocline. Typically, lead-induced plumes cannot penetrate through this pycnocline unless the Richardson number based on the plume velocity and the pycnoclinic stratification is low (Noh et al. [135]; Ching et al. [136]; Narimousa [125]). Therefore, the descending plumes usually deflect at the pycnocline and spread as gravity currents along the interface until instabilities disintegrate the current into anticyclonic eddies (Smith and Morison [137]).

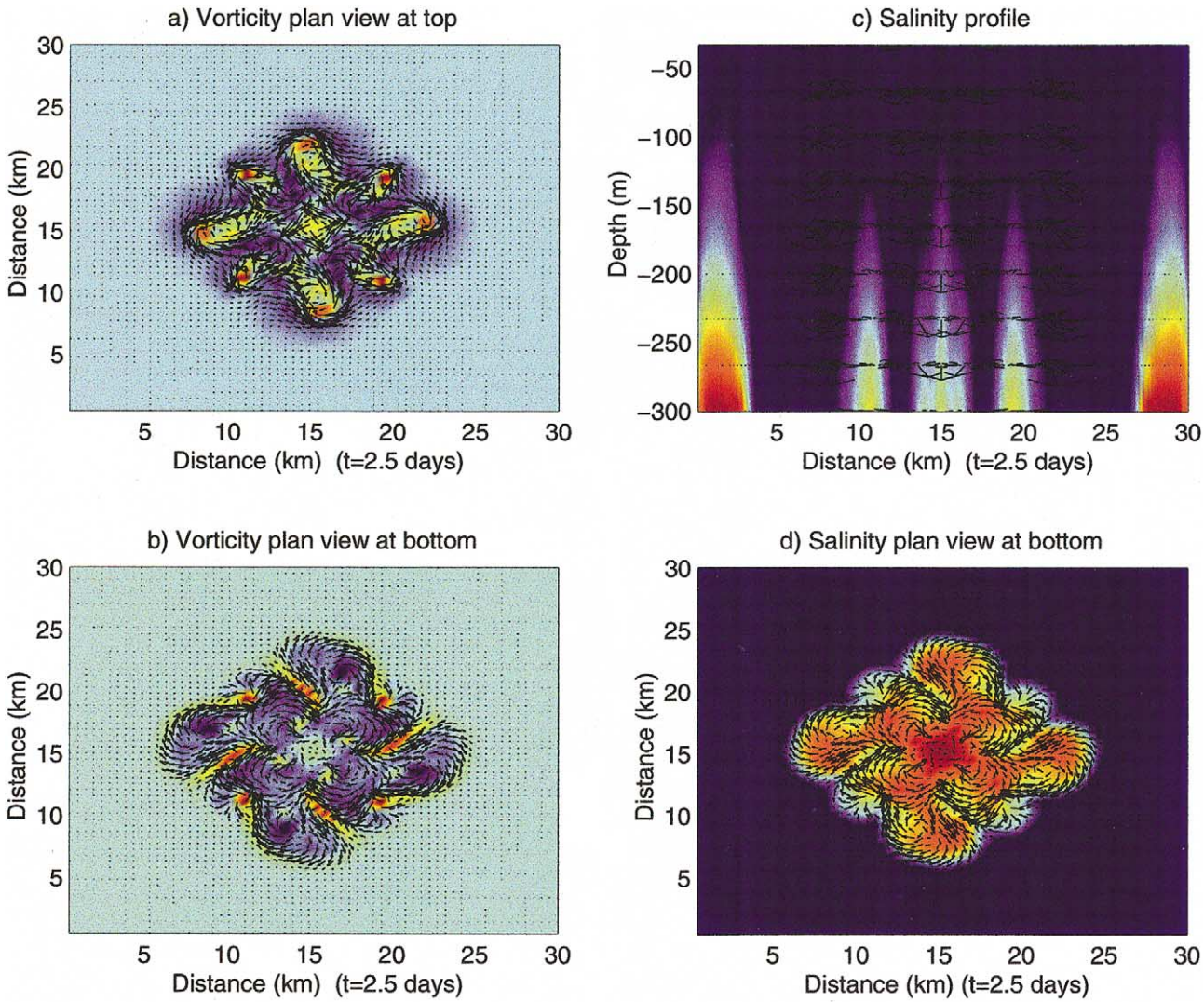

Figure 25. Non-hydrostatic numerical simulation of a 3D polynya. (a) The plan view of vorticity at the surface and (b) at a depth of 225 m. The color-coding indicates the magnitude of relative vorticity, with red and purple representing the maximum cyclonic and anticyclonic vorticities, respectively; (c) a side view of the salinity field, with the planar instantaneous (u,w) velocity field superimposed, corresponding to a cross section through the center; (d) the horizontal salinity structure at the bottom, with the distribution of horizontal velocity. Maximum vorticity anomalies are in the range $\pm 5 \times 10^{-4}$ s^{-1}. The salinity varies from 31 (blue) to 31.04 (red) ppt. The maximum horizontal and vertical velocities are 0.12 and 0.05 ms^{-1}, respectively.

Winter polar leads refreeze within several days (The LEADEX Group [138]), and hence meso-scale processes within them are of transitionary nature. Unsteadiness of lead-related processes was accounted by Bush and Woods [133,134] in their line-plume experiments carried out in both stratified (with $h_N < h_R$) and homogeneous fluids. Special conditions were maintained in these experiments, however, in that the time-scale for the emergence of eddies was maintained of the same order as the time scale of buoyancy forcing t_s. The radius of anticyclonic vortices formed were found to be $R_v \approx 0.75(q_0^l)^{1/3} t_s^{1/2} f^{-1/2}$, independent of the lead width, fluid depth H and stratification N. In homogeneous environments, the evolution of vortex structures are dependent on the magnitudes of H and h_R. When $H > h_R$, a continuously forced plume is affected by rotation

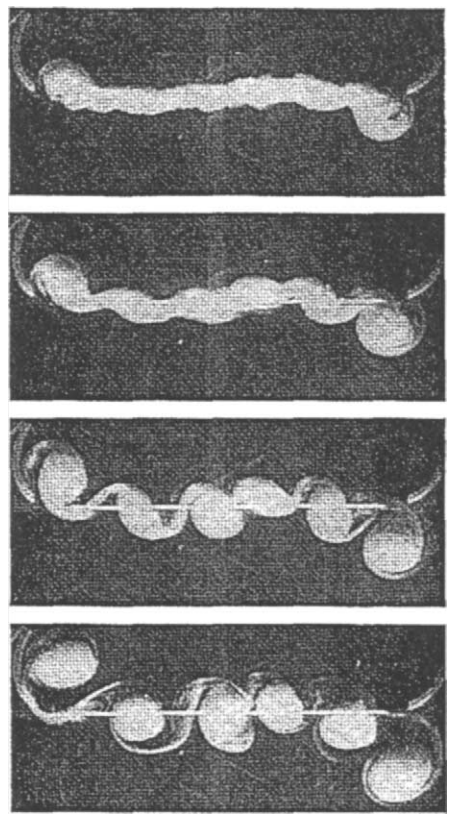

Figure 26. Formation of anticyclonic vortex structures from a line plume discharging into a rotating stratified fluid, as viewed from above. Figures (i) to (iv) represent the chronology of evolution (for details, see Bush and Woods [134]).

before it reaches the horizontal boundary and breaks down to form vortices of size $R_v \sim (q_0^l/f^3)^{1/3}$. For the case $H < h_R$, the plume reaches the boundary without rotational influence, spreads and then becomes unstable with $R_v \sim (q_0^l/f^3)^{1/3}$. When the forcing time t_s is less than the instability time scale, anticyclonic vortices emerge with $R_v \sim (q_0^l)^{1/3} t_s^{1/3} f^{-2/3}$.

Another parameter of interest is the lead width W_L. If the depth of the thermocline H is less than about $10W_L$, which is typical of polar leads, then the line plume approximation ($W_L \to 0$) breaks down and lead convection should be treated as corresponding to a source with finite width. The scaling here is fundamentally different from the line plume case and, analogous to the distributed round plume case, the velocity and buoyancy scales near the source ought to be $(q_0 W_L)^{1/3}$ and $(q_0^2/W_L)^{1/3}$, respectively. Therefore, for $H < h_R$, the emerging anticyclonic vortices are expected to have a scale proportional to the Rossby deformation radius, $R_v \sim (q_0^2 H^3/W_L f^6)^{1/6}$. The numerical experiments of Smith et al. [108] also show width dependence and indicate an eddy size of 4.0 $(q_0/f^3)^{1/2}(W/H)^{1/6}$.

In order to investigate vortex structures pertinent to lead convection, numerical simulations were carried out using the non-hydrostatic model described before with a lead of width of 720 m and a length of 12 km. The buoyancy forcing (a saline buoyancy flux of 2×10^{-7} $m^2 s^{-3}$) was applied only during the first day of simulation to mimic the finite opening time of the lead. *Figure 27* shows temporal evolution of the lead over a 6-day period. Also shown in the figure are the salinity and vorticity distributions at two-day intervals at a depth of 35 m. The initial motion occurs in the form of two counter-flowing along-lead jets with some vortex structures enclosed within, and at the lead edges the current flows with ice edge on the right. This circulation is

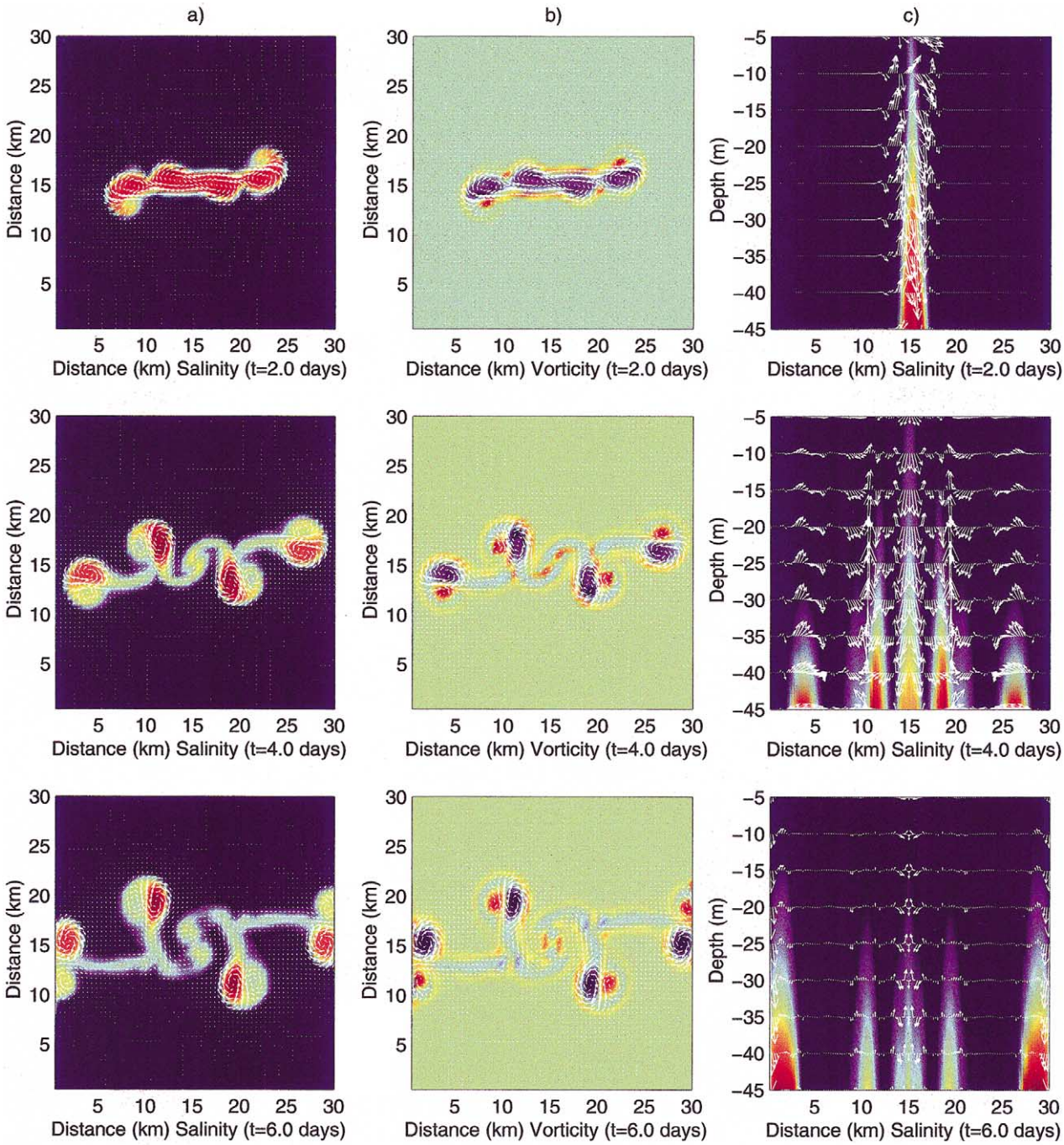

Figure 27. A simulation of a winter polar lead in a $30 \times 30 \times 0.05$ km domain. (a) The evolution of salinity in plan view at a 35 m depth on days 2, 4 and 6. The color indicates the salinity, with red corresponding to the maximum (31.04 ppt) and blue representing the background (31.0 ppt). The velocity vectors and superimposed; (b) vorticity at 35 m depth with red and blue indicating the maximum values of cyclonic and anticyclonic vorticity, respectively; (c) a side view of salinity section through the along-lead direction at the center. The maximum and minimum salinities are the same as in panel (a). The forcing took place only during the first day. The instantaneous planar velocity vectors are also superimposed.

generally cyclonic at the surface due to the converging flow and anticyclonic at the 35 m depth because of the influence of Coriolis forces on the outflow. The initial development in this experiment results in the formation of dipole pairs (radius ~ 3 km) at each end of the source region. By day 2 the flow develops an along lead instability with a wavelength of ~ 10 km. A second set of dipoles form at $x = 10$ and 20 km in *figures 27(a), (b)* and these propagate laterally away from the source region (here x is the abscissa, with $x = 0$ coinciding with a lead edge). *Figure 27(c)* shows the vertical evolution of the salt field for 2-day intervals during this same experiment. The descending line plume remains vertically coherent during the forcing period but becomes bottom trapped and anticyclonically sheared by day 2.

The dipole pair form on each end of the line plume on day 2 propagates (approximately 1 km/day) in $\pm x$ directions away from their origins. By day 3 the line plume has degenerated, through instability, into four discrete rotating dipoles, the strongest of which are anticyclones centered at $x \approx 12$ and 18 km. On day 4, these anticyclones propagate laterally in the $\pm y$ (across-lead) directions. A transient cyclone forms at $x = 15$ km in mid domain which has comparable scales to the bottom-trapped anticyclones, suggesting that it may be of origin other than instabilities due to surface forcing. This cyclone forms from the bottom up as the upward recirculating flow is stretched. This cyclone, however, fades away during the final 4 days of the simulation. The radial scale (radius) of these features is approximately 1–2 km and it is a relatively robust feature of a number of experiments. A full description of the model results will be given in a separate publication where lead width, buoyancy flux and duration of buoyancy forcing are varied (Smith et al. [108]). Anticyclones are the dominant salt containing eddies in all of those experiments.

Laboratory experiments with line plumes ($W_L \to 0$) carried out by Bush and Woods [133] indicate that the vortices generated by the outflow at depth are anticyclonic (however, the vorticity field was not fully mapped in their study). In contrast, our numerical simulations with distributed line plumes show that both anticyclonic and cyclonic vortices can evolve, often as dipole pairs. In simulated dipoles, however, the anticyclones contain stronger salinity and vorticity anomalies as evident from *figures 27(a), (b)*. It is interesting to note that Manley and Hunkins [139] have reported observations of vortices under the polar ice cover with radii on the order 10 km, with two of seven vortices being cyclonic.

6. Conclusions

The intention of this paper was to present a broad overview of the type of vortex structures that emerge during convective events in geophysical flows. Owing to the vastness of possible vortex structures, this review accommodates only a limited number of such structures, although efforts were made to cover the topic in point to the extent permissible. Convection events in environmental flows occurring over a range of length and time scales were identified and examples of intriguing vortex structures that are formed during such events, especially in the presence of background stratification and rotation, were presented. Planetary scale variations of solar radiation creates unstable thermal anomalies in the atmosphere and oceans, which break down to form smaller scales of motions that often appear as well-defined vortex structures. They include Hadley circulation, baroclinic eddies, hurricanes and thunderstorms, Hetons, tornadic vortices, microbursts and dust devils, and these vortices have significant influence on climatic to micrometeorological phenomena. Many of these vortices remain unresolved or under-resolved in environmental forecasting models, and hence their effects need to be accurately parameterized. Study of the fluid dynamics of convection in the presence of stratification, rotation and inhomogeneities not only yield useful physical and mathematical descriptions of such vortex structures of geophysical relevance, but also reveal how nature produces aesthetically appealing orderly (coherent) flow patterns on planetary scales, which become disorderly and lose memory of their origin at human-scales and finally dissipate at (Kolmogorov) microscales due to molecular friction.

Acknowledgments

We wish to thank the organizers (Professors G.J.F. van Heijst and R. Verzicco) of EUROMECH 396, "Vortex Structures in Stratified and Rotating Fluids" for giving us the opportunity to write this review. During the preparation of this manuscript, the authors were supported by the Office of Naval Research (High Latitude Dynamics Program; DCSIV), National Science Foundation (Fluid Mechanics and Hydraulics Program; HJSF), Department of Energy (Environmental Meteorology Program; HJSF), Army Research Office (Geosciences Program; HJSF) and NASA (DCSIV). The authors wish to thank Michael Levy, Destry Lucas, Gregory Cole and Richard Eijmberts for their help with the laboratory experiments and William Lavelle for his help in the numerical model development efforts.

References

[1] Rumford C., Of the propagation of heat in fluids, Am. Acad. of Arts and Sci. Complete Works, Boston, 1, 1797, 239.
[2] Siggia E.D., High Rayleigh number convection, Annu. Rev. Fluid Mech. 26 (1994) 137–168.
[3] Hunt J.C.R., Eddy dynamics and kinematics of convective turbulence, in: Plate E.J., Fedorovich E., Viegas D.X., Wyngaard J.C. (Eds.), Buoyant Convection in Geophysical Flow, Kluwer, Dordrecht, 1998.
[4] Bodenschatz E., Pesch W., Ahlers G., Recent developments in Rayleigh–Benard convection, Annu. Rev. Fluid Mech. 32 (2000) 709–778.
[5] Broecker W.S., Denton G.H., What drives glacial cycles?, Sci. Am. 262 (1990) 42–50.
[6] Eady E.T., Long waves and cyclone waves, Tellus 1 (1949) 33–52.
[7] Fultz D., Long R.R., Owens G.W., Bohan W., Kaylor R., Weil J., Studies of thermal convection in a rotating cylinder with some implications for large-scale atmospheric motions, Meterol. Monogr. 4 (1959) 1–104.
[8] Hide R., Mason P.J., Sloping convection in a rotating fluid, Adv. Phys. 24 (1975) 47–100.
[9] Hide R., Mason P.J., Plumb R.A., Thermal convection in a rotating fluid subject to a horizontal temperature gradient: spatial and temporal characteristics of fully developed baroclinic waves, J. Atmos. Sci. 34 (1977) 930–950.
[10] Buzyna G., Pfeffer R.L., Kung R., Transition to geostrophic turbulence in a rotating differentially heated annulus of fluid, J. Fluid Mech. 145 (1984) 377–403.
[11] Park Y.-G., Whitehead J.A., Rotating convection driven by differential bottom heating, J. Phys. Oceanogr. 29 (1999) 1208–1220.
[12] Kim E.-J., Hughes D.W., Soward A.M., An investigation into high conductivity dynamo action driven by rotating convection, Geophys. Astrophys. Fluid Dyn. 91 (1999) 303–332.
[13] Griffiths R.W., Effects of Earth's rotation on convection in magma chambers, Earth Planet. Sc. Lett. 85 (1987) 525–536.
[14] Davis J., Dynamic Earth: Plates, Plumes and Mantle Convection, Cambridge University Press, 2000.
[15] Smith S.D., Muench R.D., Pease C.H., Polynyas and leads: an overview of physical processes and environment, J. Geophys. Res. 95 (C6) (1990) 9461–9479.
[16] Morison J.H., McPhee M., Curtin T., Paulson C., The oceanography of leads, J. Geophys. Res. 97 (C7) (1992) 11199–11218.
[17] Maxworthy T., Convection into domains with open boundaries, Annu. Rev. Fluid Mech. 29 (1997) 327–371.
[18] Fujita T.T., DFW Microburst on August 2, 1985, University of Chicago, 1986.
[19] Speer K.G., Rona P.A., A model of an Atlantic and Pacific hydrothermal plume, J. Geophys. Res. 94 (1989) 6213–6220.
[20] German C.R., Baker E.T., Mevel C., Tamaki K., The FUJI science team, hydrothermal activity along the southwest Indian ridge, Nature 395 (1998) 490–493.
[21] Lavelle J.W., Wetzler M.A., Diffuse venting and background contributions to chemical anomalies in a neutrally buoyant ocean hydrothermal plume, J. Geophys. Res. 104 (C2) (1999) 3201–3209.
[22] Rayleigh J.W.S., On convective currents in a horizontal layer of fluid when the higher temperature is on the under side, Phil. Mag. 32 (1916) 529–546.
[23] Chandrasekhar S., Hydrodynamic and Hydromagnetic Stability, Clarendon Press, Oxford, 1961.
[24] Thomson J., On a changing tessellated structure in certain liquids, P. Phil. Soc. Glasgow 13 (1882) 464–468.
[25] Koschmieder E.L., On the wavelength of convective motions, J. Fluid Mech. 35 (1969) 527–530.
[26] Koschmieder E.L., Benard convection, in: Rice S.A., Prigogine I. (Eds.), Adv. Chem. Phys., Vol. 26, Wiley-Interscience, 1974, pp. 177–212.
[27] Theerthan S.A., Arakeri J.H., Planform structure and heat transfer in turbulent free convection over horizontal surfaces, Phys. Fluids 12 (4) (2000) 884–894.
[28] Sasaki Y., Influences of thermal boundary layer on atmospheric cellular convection, J. Meteorol. Soc. Japan 48 (1970) 492–502.
[29] Busse F.H., Nonlinear properties of thermal convection, Rep. Prog. Phys. 41 (1978) 1931–1967.
[30] Riahi N., Nonlinear thermal convection with finite conducting boundaries, J. Fluid Mech. 152 (1984) 113–123.
[31] Fiedler B.H., Thermal convection in a layer bounded by uniform heat flux: Application of a strongly non-linear analytical solution, Geophys. Astro. Fluid Dyn. 91 (1999) 223–250.

[32] Getling A.V., Evolution of two-dimensional disturbances in the Rayleigh–Benard problem and their preferred wave numbers, J. Fluid Mech. 130 (1983) 165–186.
[33] Chapman, C.J., Proctor M.R.E., Non-linear Rayleigh–Benard convection between poorly conducting boundaries, J. Fluid Mech. 101 (1980) 759–782.
[34] Rothermel J., Agee E.M., A numerical study of atmospheric convective scaling, J. Atmos. Sci. 43 (1986) 1185–1197.
[35] Van Delden A., Scale selection in low-order spectral models of two-dimensional thermal connection, Tellus 36A (1984) 458–479.
[36] Lorenz E.N., Deterministic non-periodic flow, J. Atmos. Sci. 20 (1963) 130–141.
[37] Krishnamurty R., On the transition to turbulent convection II: The transition to turbulent time-dependent flow, J. Fluid Mech. 42 (1970) 295–302.
[38] Willis G.E., Deardorff J.W., A laboratory model of the unstable planetary boundary layer, J. Atmos. Sci. 31 (1974) 1297–1307.
[39] Willis G.E., Deardorff J.W., Visual observations of horizontal planforms of penetrative convection, in: Proc. Third Symp. Atmos. Tur., Diff. and Air Qual., Amer. Meteorol. Soc., Boston, MA, 1976.
[40] Willis G.E., Deardorff J.W., Laboratory observations of turbulent penetrative-convection planforms, J. Geophys. Res. 84 (C1) (1979) 295–302.
[41] Busse F.H., Whitehead J.A., Oscillatory and convective instabilities in large Prandtl number convection, J. Fluid Mech. 66 (1974) 67–79.
[42] Katsoros K.B., Turbulent free convection in fresh and salt water: Some characteristics revealed by visualization, J. Phys. Oceanogr. 8 (1978) 613–626.
[43] Cole G.S., Fernando H.J.S., Some aspects of the decay of convective turbulence, Fluid Dyn. Res. 23 (1998) 161–176.
[44] Niemela J.J., Skrbek L., Sreenivasan K.R., Donnelly R.J., Turbulent convection at very high Rayleigh numbers, Nature 404 (2000) 837–840.
[45] Kaimal J.C., Wyngaard J.C., Haugen D.A., Cote O.R., Izumi Y., Caughey S.J., Readings C.J., Turbulence structure in the convective boundary layer, J. Atmos. Sci. 33 (1976) 2153–2169.
[46] Kerr R.M., Rayleigh number scaling in numerical convection, J. Fluid Mech. 310 (1996) 139–179.
[47] Sullivan P.P., Moeng C.H., Stevens B., Lenschow D.H., Mayor S.D., Structure of the entrainment zone capping the convective atmospheric boundary layer, J. Atmos. Sci. 55 (1998) 3042–3064.
[48] Jeffreys H., Some cases of instability in fluid motion, Proc. Roy. Soc. Lond. A 118 (1928) 195–208.
[49] Nakagawa Y., Frenzen P., A theoretical and experimental study of cellular convection in rotating fluids, Tellus 7 (1955) 1–21.
[50] Julien K., Knobloch E., Fully non-linear three-dimensional convection in a rapidly rotating layer, Phys. Fluids 11 (6) (1999) 1469–1483.
[51] Adrian R.J., Ferreira R.T.D.S., Boberg T., Turbulent thermal convection in wide horizontal fluid layers, Exp. Fluids 4 (1986) 121–141.
[52] Martinet B., Adrian R.J., Rayleigh–Benard convection; experimental study of time dependednt instabilities, Exp. Fluids 6 (1988) 316–322.
[53] Foster T.D., Intermittent convection, Geophys. Fluid Dyn. 2 (1971) 201–217.
[54] Foster T.D., Waller S., Experiments on convection at very high Rayleigh numbers, Phys. Fluids 28 (2) (1985) 455–461.
[55] Willis G.E., Deardorff J.W., The oscillatory motions of Rayleigh convection, J. Fluid Mech. 44 (1970) 661–672.
[56] Howard L.N., Convection at high Rayleigh number, in: Gortler H. (Ed.), Proc. Eleventh Int. Congress App. Mech., Munich, 1964, pp. 1109–1115.
[57] Sparrow E.M., Husar R.B., Goldstein R.J., Observations and other characteristics of thermals, J. Fluid Mech. 41 (1970) 793.
[58] Ginzburg A.I., Golitsyn G.S., Fedorov K.N., Measurements of convection time scale in water at its cooling from the surface, Izv. Atmos. Oceanic. Phys. 15 (1979) 333–335.
[59] Katsoros K.B., Liu W.T., Businger J.A., Tillman J.E., Heat transport and thermal structure in the interfacial boundary layer measured in an open tank of water in turbulent free convection, J. Fluid Mech. 83 (1977) 311–335.
[60] Maxworthy T., A vorticity source for large-scale dust devils and other comments on naturally occurring columnar vortices, J. Atmos. Sci 30 (1971) 1717–1721.
[61] Klemp J.B., Dynamics of the tornadic thunderstorms, Annu. Rev. Fluid Mech. 19 (1987) 369–402.
[62] Sinclair P.C., On the rotation of dust devils, B. Am. Meteorol. Soc. 46 (1965) 388–391.
[63] Fernando H.J.S., Buoyancy transfer across a diffusive interface, J. Fluid Mech. 209 (1989) 1–34.
[64] Akitomo K., Imasato N., Yamashita S.I., A numerical study on scale selection of convection in a shallow sea, Cont. Shelf. Res. 12 (4) (1992) 451–469.
[65] Dalziel S.B., Rayleigh–Taylor instability: Experiments with image analysis, Dynam. Atmos. Oceans 20 (1993) 127–153.
[66] Deardorff J.W., Preliminary results from numerical investigations of the unstable boundary layer, J. Atmos. Sci. 27 (1970) 1209–1211.
[67] Fernando H.J.S., Boyer D.L., Chen R.-R., Turbulent thermal convection in rotating stratified fluids, Dynam. Atmos. Oceans 13 (1989) 95–121.
[68] Cenedese A., Querzoli G., Lagrangian study of the convective boundary layer using the image analysis, in: Proceedings of the 7th Symposium on Applications of Laser Techniques to Fluid Mechanics, 1993, pp. 22.1.1–22.1.7.
[69] Hunt J.C.R., Turbulence structure in thermal convection and shear-free boundary layers, J. Fluid Mech. 138 (1984) 161–184.
[70] Kit E.L., Strang E.J., Fernando H.J.S., Measurement of turbulence near shear-free density interfaces, J. Fluid Mech. 334 (1997) 293–314.
[71] Hardy K.R., Otterson H., Radar investigation of convective patterns in the clear atmosphere, J. Atmos. Sci. 26 (1969) 666–672.
[72] Linden P.F., The deepening of a mixed layer in a linearly stratified fluid, J. Fluid Mech. 71 (1975) 385–405.
[73] Carruthers D.J., Hunt J.C.R., Waves, turbulence and entrainment near an inversion layer, J. Fluid Mech. (2000) submitted.
[74] Carruthers D.J., Moeng C.H., Waves in the overlying inversion of the convective boundary layer, J. Atmos. Sci. 44 (14) (1987) 1801–1808.
[75] Perera M.J.A.M., Fernando H.J.S., Boyer D.L., Turbulent mixing at an inversion layer, J. Fluid Mech. 267 (1994) 275–298.
[76] McGrath J., Fernando H.J.S., Hunt J.C.R., Turbulence waves and mixing at shear-free density interfaces. Part: 2 Laboratory experiments, J. Fluid Mech. 347 (1997) 235–261.

[77] E X., Hopfinger E.J., On mixing across an interface in stably stratified fluid, J. Fluid Mech. 166 (1986) 227–244.
[78] Deardorff J.W., Willis G.E., Lilly D.K., Laboratory Investigation of non-steady penetrative convection, J. Fluid Mech. 35 (1969) 7–31.
[79] Deardorff J.W., Willis G.E., Stockton B.H., Laboratory studies of entrainment zone of a convective mixed layer, J. Fluid Mech. 100 (1980) 41–62.
[80] Rossby, A study of Benard convection with and without rotation, J. Fluid Mech. 36 (1969) 309–335.
[81] Bajaj K.M.S., Jun L., Naberhuis B., Ahlers G., Square patterns in Rayleigh–Benard convection with rotation about a vertical axis, Phys. Rev. Let. 81 (4) (1998) 806–809.
[82] Boubnov B.M., Golitsyn G.S., Thermal turbulence and rotation, RJCM 1 (1) (1993) 59–70.
[83] Hu Y., Ecke R.E., Ahlers G., Time and length scales in rotating Rayleigh–Benard convection, Phys. Rev. Lett. 74 (25) (1995) 5040–5043.
[84] Cox S.M., Matthews P.C., Instability of rotating convection, J. Fluid Mech. 403 (2000) 153–172.
[85] Boubnov B.M., Golitsyn G.S., Experimental study of convective structures in rotating fluids, J. Fluid Mech. 167 (1986) 503–531.
[86] Boubnov B.M., Golitsyn G.S., Temperature and velocity field regimes of convective motions in a rotating plane fluid layer, J. Fluid Mech. 219 (1990) 215–239.
[87] Fultz D., Some cases of instability in cylindrically symmetric flows, in: 9th Midwestern Mechanics Conference, Wisconsin, Madison, Aug 16–18, 1965, pp. 37–48.
[88] Long R.R., Note on Taylor's "ink walls" in a rotating fluid, J. Meteor. 11 (3) (1954) 247–249.
[89] Sakai S., The horizontal scale of rotating convection in the geostrophic regime, J. Fluid Mech. 333 (1997) 85–95.
[90] Golitsyn G.S., Simple theoretical and experimental study of convection with some geophysical applications and analogies, J. Fluid Mech. 95 (1979) 567–608.
[91] Chen R., Fernando H.J.S., Boyer D.L., Formation of isolated vortices in a rotating convecting fluid, J. Geophys. Res. 94 (D15) (1989) 18,445–18,453.
[92] Brickman D., Kelley D.E., Development of convection in a rotating fluid: Scales and patterns of motion, Dynam. Atmos. Oceans 19 (1993) 389–405.
[93] Julien K., Legg S., McWilliams J., Werne J., Plumes in rotating convection. Part 1. Ensemble statistics and dynamical balances, J. Fluid Mech. 391 (1999) 151–187.
[94] Heslot F., Castaing B., Libchaber A., Transitions to turbulence in helium gas, Phys. Rev. A 36 (1987) 5870–5873.
[95] Castaing B., Gunaratne G., Heslot F., Kadanoff L., Libchaber A., Thomae S., Wu X.-Z., Zaleski S., Zanetti G., Scaling of hard thermal turbulence in Rayleigh–Benard convection, J. Fluid Mech. 204 (1989) 1–30.
[96] Turner J.S., The motion of buoyant elements in turbulent surroundings, J. Fluid Mech. 16 (1963) 1–16.
[97] Ching C.Y., Fernando H.J.S., Robles A., Breakdown of line plumes in turbulent environments, J. Geophys. Res. 100 (C3) (1995) 4707–4713.
[98] Fernando H.J.S., Chen R.-R., Boyer D.L., Effects of rotation on convective turbulence, J. Fluid Mech. 228 (1991) 513–547.
[99] Ivey G.N., Taylor J.R., Coates M.J., Convectively driven mixed layer growth in a rotating stratified fluid, Deep Sea Res. 42 (1995) 331–349.
[100] Coates M.J., Ivey G.N., On convective turbulence and the influence of rotation, Dynam. Atmos. Oceans 25 (1997) 217–232.
[101] Marshall J.C., Schott F., Open-ocean convection: Observations, theory and models, Report #52, Center for Global Change Science, MIT, 1998.
[102] Levy M.A., Fernando H.J.S., Turbulent convection in rotating stratified fluids, J. Fluid Mech. (2000), submitted.
[103] Hart J.E., Ohlsen D.R., On the thermal offset in turbulent rotating convection, Phys. Fluids 11 (8) (1999).
[104] D'Asaro E., Farmer D., Osse J., Dairiki, A Lagrangian float, J. Atmos. Oceanic Tech. 13 (1996) 1230–1246.
[105] Julien K., Legg S., McWilliams J., Werne J., Penetrative convection in rapidly rotating flows: Preliminary results from numerical simulations, Dynam. Atmos. Oceans 24 (1996) 237–250.
[106] Smith D.C., Morison J.H., Nonhydrostatic haline convection under leads in sea ice, J. Geophys. Res. 103 (C2) (1998) 3233–3247.
[107] Brugge R., Jones H.L., Marshall J.C., Non-hydrostatic ocean modeling for studies of open ocean deep convection, in: Deep Convection and Water Formation in Oceans, Elsevier Oceanographic Series, 1991, pp. 325–340.
[108] Smith D.C. IV, Lavelle J.W., Fernando H.J.S., Arctic ocean mixed layer eddy generation under leads in sea ice, submitted, 2001.
[109] Lavelle J.W., Smith D.C., Effects of rotation on convection plumes from line segment sources, J. Phys. Oceanogr. 26 (1996) 863–872.
[110] Fischer H., List J., Koh R., Imberger J., Brooks N., Mixing in Inland and Coastal Waters, Academic Press, 1979.
[111] List E.J., Turbulent jets and plumes, Annu. Rev. Fluid Mech. 14 (1982) 189–211.
[112] Turner J.S., Turbulent entrainment: The development of the entrainment assumption and its application to geophysical flows, J. Fluid Mech. 173 (1986) 431–471.
[113] Davies P.A., Neves M.J., Recent research advances in the fluid mechanics of turbulent jets and plumes, NATO ASI Ser., Ser. E 255, 1994.
[114] Morton B.R., Taylor G.I., Turner J.S., Turbulent gravitational convection from maintained and instantaneous sources, P. Roy. Soc. Lond. A 234 (1956) 1–23.
[115] Fernando H.J.S., Chen R.-R., Ayotte B.A., Development of a point plume in the presence of background rotation, Phys. Fluids 10 (9) (1998) 2369–2383.
[116] Boubnov B.M., van Heijst G.J.F., Experiments on convection from a horizontal plate with and without background rotation, Exp. Fluids 16 (1994) 155–164.
[117] Speer K.G., Marshall J., The growth of convective plumes of seafloor hotsprings, J. Mar. Res. 53 (1995) 1025–1057.
[118] Ayotte B.A., Fernando H.J.S., The motion of a turbulent thermal in the presence of background rotation, J. Atmos. Sci. 51 (13) (1994) 1989–1994.
[119] Helfrich K.R., Thermals with background rotation and stratification, J. Fluid Mech. 259 (1994) 265–280.

[120] Helfrich K.R., Battisti D., Experiments on baroclinic vortex shedding from hydrothermal plumes, J. Geophys. Res. 96 (1991) 12,511–12,518.
[121] Hogg N.G., Stommel H.M., The heton, an elementary interaction between discrete baroclinic geostrophic vortices, and its implications concerning eddy heat-flow, P. Roy. Soc. Lond. A 397 (1985) 1–20.
[122] Colomer J., Boubnov B.M., Fernando H.J.S., Turbulent convection from isolated sources, Dynam. Atmos. Oceans 30 (1999) 125–148.
[123] Jones H., Marshall J., Convection with rotation in a neutral ocean; A study of open-ocean deep convection, J. Phys. Oceanogr. 23 (1993) 1009–1039.
[124] Maxworthy T., Narimousa S., Unsteady, turbulent convection into a homogeneous, rotating fluid, with oceanographic applications, J. Phys. Oceanogr. 24 (1994) 865–887.
[125] Narimousa S., Penetrative, turbulent convection into a rotating, two-layer fluid, J. Fluid Mech. 312 (1996) 299–313.
[126] Whitehead J.A., Marshall J., Hufford G.E., Localized convection in rotating stratified fluid, J. Geophys. Res. 101 (C10) (1996) 25270–25271.
[127] Visbeck M., Marshall J., Jones H., Dynamics of isolated convective regions in the ocean, J. Phys. Oceanogr. 26 (1996) 1723–1734.
[128] Colomer J., Zieren L.D., Fernando H.J.S., Comment on 'Localized convection in rotating stratified fluid', J. Geophys. Res. 103 (C6) (1998) 12,891–12,894.
[129] Legg S., Marshall J., A heton model of the spreading phase of open-ocean deep convection, J. Phys. Oceanogr. 23 (1993) 1040–1056.
[130] Fernando H.J.S., Ching C.Y., Lead-induced convection: a laboratory perspective, J. Marine Syst. 4 (1993) 217–230.
[131] Fernando H.J.S., Ching C.Y., Effects of background rotation on turbulent line plumes, J. Phys. Oceanogr. 23 (9) (1993) 2125–2129.
[132] Bush J.W.M., Woods A.W., Experiments on buoyant plumes in a rotating channel, Geophys. Astro. Fluid 89 (1998) 1–22.
[133] Bush J.W.M., Woods A.W., Vortex generation by line plumes in a rotating stratified fluid, J. Fluid Mech. 388 (1999) 289–313.
[134] Bush J.W.M., Woods A.W., An investigation of the link between lead-induced thermohaline convection and arctic eddies, Gephys. Res. Lett. 27 (8) (2000) 1179–1182.
[135] Noh Y., Fernando H.J.S., Ching C.Y., Flows induced by the impingement of a two dimensional thermal on a density interface, J. Phys. Oceanogr. 22 (1992) 1207–1220.
[136] Ching C.Y., Fernando H.J.S., Noh Y., Interaction of a negatively buoyant plume with a density interface, Dynam. Atmos. Oceans 19 (1993) 367–388.
[137] Smith D.C., Morison J.H., A numerical study of haline convection beneath leads in sea ice, J. Geophys. Res. 98 (1993) 10069–10083.
[138] The LEADEX Group, The Leadex experiment, Eos 74 (35) (1993) 393, 396–397.
[139] Manley T.O., Hunkins K., Mesoscale eddies of the Arctic ocean, J. Geophys. Res. 90 (C3) (1985) 4911–4930.